

---

**Supplementary information**

---

# **Stabilization and operation of a Kerr-cat qubit**

---

In the format provided by the  
authors and unedited

# SUPPLEMENTARY INFORMATION

## I. GENERAL ENCODING

In this section, we define the general cat-qubit Bloch sphere following the conventions of Ref. [1] in terms of the eigenstates of Hamiltonian  $\hat{H}_{\text{cat}}$  (1) without the approximation that  $|\langle +\alpha | -\alpha \rangle| = e^{-2\bar{n}} \ll 1$  where  $\bar{n} = |\alpha|^2$  as used in the main text of the paper. It has been shown [2] that the two states  $|\mathcal{C}_\alpha^\pm\rangle = \mathcal{N}_\alpha^\pm (|+\alpha\rangle \pm |-\alpha\rangle)$  are degenerate eigenstates of  $\hat{H}_{\text{cat}}$ , where  $\alpha = \sqrt{\epsilon_2/K}$  is the amplitude of the coherent states in the superposition and  $\mathcal{N}_\alpha^\pm = 1/\sqrt{2(1 \pm e^{-2\bar{n}})}$  is the normalization coefficient to account for  $|\langle +\alpha | -\alpha \rangle| \neq 0$ . These expressions are valid for all  $\epsilon_2/K$ , and in the limit  $\epsilon_2/K \rightarrow 0$  they become  $|\mathcal{C}_\alpha^+\rangle \rightarrow |n=0\rangle$  and  $|\mathcal{C}_\alpha^-\rangle \rightarrow |n=1\rangle$ . This validates the adiabatic mapping between the Fock-qubit and cat-qubit Bloch spheres, which share a common definition  $|\pm Z\rangle = |\mathcal{C}_\alpha^\pm\rangle$  for their respective values of  $\alpha$ .

The definitions relating the general encoding to the Bloch sphere of Fig. 1a in the limit  $p = \mathcal{N}_\alpha^+/\mathcal{N}_\alpha^- \rightarrow 1$  are:

$$|\pm X\rangle = (|\mathcal{C}_\alpha^+\rangle \pm |\mathcal{C}_\alpha^-\rangle)/\sqrt{2} \rightarrow |\pm\alpha\rangle \quad (\text{S1})$$

$$|\pm Y\rangle = (|\mathcal{C}_\alpha^+\rangle \pm i|\mathcal{C}_\alpha^-\rangle)/\sqrt{2} \rightarrow (|+\alpha\rangle \mp i|-\alpha\rangle)/\sqrt{2} = |\mathcal{C}_\alpha^{\mp i}\rangle \quad (\text{S2})$$

$$|\pm Z\rangle = |\mathcal{C}_\alpha^\pm\rangle \rightarrow (|+\alpha\rangle \pm |-\alpha\rangle)/\sqrt{2} \quad (\text{S3})$$

This limit, where the coherent states  $|\pm\alpha\rangle$  are orthogonal, is reached exponentially fast with  $\bar{n} = |\alpha|^2$ . For the photon numbers used in this work,  $\bar{n} = 2.2$  (Fig. 2c,d,e) and  $\bar{n} = 2.6$  (Fig. 3,4) the associated values are  $p \approx 0.988$  and  $p \approx 0.994$ . It is in this sense that  $|\pm X\rangle \approx |\pm\alpha\rangle$  are macroscopically distinct states, which translates to a protection of the degeneracy of  $|\pm Y\rangle$  and  $|\pm Z\rangle$  against locally correlated noisy environments, or equivalently the suppression of phase flips.

This suppression also becomes evident by expressing the action of the photon-loss jump operator  $\hat{a}$  on the states of the cat-qubit Bloch sphere:

$$\hat{a} = \alpha [p^{-1} |\mathcal{C}_\alpha^+\rangle \langle \mathcal{C}_\alpha^-| + p |\mathcal{C}_\alpha^-\rangle \langle \mathcal{C}_\alpha^+|] \quad (\text{S4})$$

$$= \alpha \left[ \frac{p^{-1} + p}{2} \hat{\sigma}_x + \frac{p^{-1} - p}{2} i \hat{\sigma}_y \right] \quad (\text{S5})$$

where  $\hat{\sigma}_x = |\mathcal{C}_\alpha^+\rangle \langle \mathcal{C}_\alpha^-| + |\mathcal{C}_\alpha^-\rangle \langle \mathcal{C}_\alpha^+|$  and  $\hat{\sigma}_y = -i(|\mathcal{C}_\alpha^+\rangle \langle \mathcal{C}_\alpha^-| - |\mathcal{C}_\alpha^-\rangle \langle \mathcal{C}_\alpha^+|)$  are the Pauli operators acting on the states defined above. For the photon numbers presented in this work the prefactors are  $(p^{-1} + p)/2 \approx 1$  and  $(p^{-1} - p)/2 \approx 0.01$  validating the approximations made in the analytical treatments in main text and in some sections of this supplementary information. Throughout this work we use the general encoding for numerical simulations.

Finally, we point out that two conventions for the orientation of the cat-qubit encoding on the Bloch-sphere are used in the literature. One is described above and used in this work. The other convention corresponds to the application of a ninety-degree rotation (or a Hadamard gate) to the basis states of our encoding such that the coherent states are along the Z-axis and the even and odd cat states  $|\mathcal{C}_\alpha^\pm\rangle$  are along the X-axis of the new encoded qubit Bloch sphere [3, 4]. In both conventions bit-flips are defined as stochastic  $\pi$ -rotations around the X-axis and phase-flips as stochastic  $\pi$ -rotations around the Z-axis [5]. Consequently, there is a difference in which of the two error channels is suppressed: In our encoding the phase-flip error channel is suppressed. Under the other convention it is the bit-flip error channel. This difference in convention is only a matter of convenience of nomenclature and does not change the error-protection capabilities of the cat-qubit.

## II. FULL SYSTEM HAMILTONIAN

Here we derive the effective system Hamiltonian from the combination of a nonlinear resonator (the Kerr-cat mode), a harmonic oscillator (the readout cavity) and several drives generating the parametric interactions used in this work. We start with the Hamiltonian

$$\hat{H}_0 = \hat{H}_a + \hat{H}_b + \hat{H}_c + \hat{H}_{\text{drives}}.$$

The first term on the right-hand side of this equation is the Hamiltonian of the nonlinear resonator given by  $\hat{H}_a/\hbar = \omega_{a,0} \hat{a}_0^\dagger \hat{a}_0 + g_3 (\hat{a}_0^\dagger + \hat{a}_0)^3 + g_4 (\hat{a}_0^\dagger + \hat{a}_0)^4$  with annihilation operator  $\hat{a}_0$ , frequency  $\omega_{a,0}$ , third-order

nonlinearity  $g_3$  and fourth-order nonlinearity  $g_4$  [6]. The second term  $\hat{H}_b/\hbar = \omega_{b,0}\hat{b}_0^\dagger\hat{b}_0$  describes the readout cavity as a harmonic oscillator with frequency  $\omega_{b,0}$  and annihilation operator  $\hat{b}_0$ . The third term  $\hat{H}_c/\hbar = g(\hat{a}_0^\dagger + \hat{a}_0)(\hat{b}_0^\dagger + \hat{b}_0)$  gives the coupling of strength  $g$  between the two modes. Finally, the last term  $\hat{H}_{\text{drives}}/\hbar = 2\text{Re}(e^{i\omega_s t})(\epsilon_s\hat{a}_0^\dagger + \epsilon_s^*\hat{a}_0) + 2\text{Re}(e^{i\omega_{\text{cr}} t})(\epsilon_{\text{cr}}\hat{a}_0^\dagger + \epsilon_{\text{cr}}^*\hat{a}_0)$  corresponds to two drives at respective frequencies  $\omega_s$  and  $\omega_{\text{cr}}$  and slowly varying complex envelopes  $\epsilon_s$  and  $\epsilon_{\text{cr}}$ . The first drive will generate the effective single-mode squeezing used for stabilization and the second one will implement the effective resonant interaction used for cat-quadrature readout. Here we have, without loss of generality, assumed that the drives address the nonlinear resonator.

After bringing  $\hat{H}_c$  into the Jaynes-Cummings form and performing the transformation  $\hat{a}_0 = \hat{a}_1 + (g/\Delta)\hat{b}_1$ ,  $\hat{b}_0 = \hat{b}_1 - (g/\Delta)\hat{a}_1$ , where  $\Delta = \omega_{b,0} - \omega_{a,0}$ , the system Hamiltonian becomes

$$\hat{H}_1/\hbar = \omega_a\hat{a}_1^\dagger\hat{a}_1 + \omega_b\hat{b}_1^\dagger\hat{b}_1 + g_3(\hat{f}_1 + \hat{f}_1^\dagger)^3 + g_4(\hat{f}_1 + \hat{f}_1^\dagger)^4 + 2\text{Re}(e^{i\omega_s t})(\epsilon_s\hat{f}_1^\dagger + \epsilon_s^*\hat{f}_1) + 2\text{Re}(e^{i\omega_{\text{cr}} t})(\epsilon_{\text{cr}}\hat{f}_1^\dagger + \epsilon_{\text{cr}}^*\hat{f}_1),$$

with the new frequencies  $\omega_a = \omega_{a,0} - 2g^2/\Delta$  and  $\omega_b = \omega_{b,0} + 2g^2/\Delta$  as well as  $\hat{f}_1 = \hat{a}_1 + (g/\Delta)\hat{b}_1$ . Since the two drives are independent and in particular the drive at frequency  $\omega_{\text{cr}}$  is not always on, we separately perform two successive transformations to a displaced frame [7] for each mode. These transformations are given by  $\hat{a}_1 = \hat{a}_2 + \xi_{a,s}(t)$ ,  $\hat{a}_2 = \hat{a}_3 + \xi_{a,\text{cr}}(t)$ ,  $\hat{b}_1 = \hat{b}_2 + \xi_{b,s}(t)$ , and  $\hat{b}_2 = \hat{b}_3 + \xi_{b,\text{cr}}(t)$ , where the displacement amplitudes are chosen [7] such that the Hamiltonian takes on the more compact form

$$\hat{H}_{\text{disp}}/\hbar = \omega_a\hat{a}_3^\dagger\hat{a}_3 + \omega_b\hat{b}_3^\dagger\hat{b}_3 + g_3\hat{f}^3 + g_4\hat{f}^4,$$

with  $\hat{f} = \hat{a}_3 + \xi_{a,s}(t) + \xi_{a,\text{cr}}(t) + (g/\Delta)(\hat{b}_3 + \xi_{b,s}(t) + \xi_{b,\text{cr}}(t)) + \text{h.c.} = \hat{a}_3 + (g/\Delta)\hat{b}_3 + \tilde{\xi}_{\text{eff},s}(t) + \tilde{\xi}_{\text{eff},\text{cr}}(t) + \text{h.c.}$ . For our system parameters, the sum and difference frequencies  $|\omega_i \pm \omega_j|/2\pi$  for  $i \in \{s, \text{cr}\}$  and  $j \in \{a, b\}$  are all larger or equal to  $\approx 3$  GHz, making them significantly larger than the loss rates of either mode  $\kappa_a/2\pi \approx 10$  kHz and  $\kappa_b/2\pi \approx 2$  MHz. Moreover  $(g/\Delta)^2 \approx 0.01 \ll 1$  (see section VII). Under these conditions the effective displacement amplitudes for  $i \in \{s, \text{cr}\}$  are

$$\tilde{\xi}_{\text{eff},i}(t) \approx \left[ \frac{\epsilon_i}{\omega_i - \omega_a} - \frac{\epsilon_i^*}{\omega_i + \omega_a} \right] e^{-i\omega_i t} = \xi_{\text{eff},i} e^{-i\omega_i t},$$

where  $\epsilon_i$  and thus  $\xi_{\text{eff},i}$  varies slowly with respect to  $|\omega_i - \omega_a|$ . In practice, with the exception of initial and final ramps and the  $Z(\pi/2)$ -gate,  $\epsilon_i$  is constant in our experiment. Note that, as opposed to the case of parametric processes generated with four-wave mixing, we cannot neglect the second term in the above expression as the tone applied to generate the parametric processes is far detuned from the mode frequency.

We now go into the rotating frames defined by  $\hat{a}_3 = \hat{a}e^{-i\frac{\omega_s}{2}t}$  and  $\hat{b}_3 = \hat{b}e^{-i\omega_b t}$ , expand the the nonlinear terms and perform the rotating wave approximation for  $\frac{\omega_s}{2} \approx \omega_a$  and  $\omega_{\text{cr}} = \omega_b - \frac{\omega_s}{2}$ . This yields the full system Hamiltonian,

$$\hat{H}/\hbar = \Delta_{as}\hat{a}^\dagger\hat{a} - K\hat{a}^{\dagger 2}\hat{a}^2 + \epsilon_2\hat{a}^{\dagger 2} + \epsilon_2^*\hat{a}^2 - \chi_{ab}\hat{a}^\dagger\hat{a}\hat{b}^\dagger\hat{b} - 4K\hat{a}^\dagger\hat{a}(|\xi_{\text{eff},s}|^2 + |\xi_{\text{eff},\text{cr}}|^2) + g_{\text{cr}}\hat{a}^\dagger\hat{b} + g_{\text{cr}}^*\hat{a}\hat{b}^\dagger \quad (\text{S6})$$

In the above expression, the first term represents a detuning between half the frequency of the tone generating the effective squeezing drive and the undriven mode frequency given by  $\Delta_{as} = \omega_a - \frac{\omega_s}{2}$ , the second term is the Kerr nonlinearity with  $K = -6g_4$ , and the third and fourth terms are the squeezing drive of strength  $\epsilon_2 = 3g_3\xi_{\text{eff},s}$ . The fifth term is the cross-Kerr interaction of strength  $\chi_{ab} = -24g_4(\frac{g}{\Delta})^2$  between the nonlinear resonator and the readout cavity used for dispersive readout of the Fock qubit. The next two terms are Stark shifts of the nonlinear resonator due to the two applied tones. The last two terms are the generated effective resonant interaction  $g_{\text{cr}} = 6g_3\frac{g}{\Delta}\xi_{\text{eff},\text{cr}}^*$  between the two modes used for cat-quadrature readout. Here we have assumed that the Stark shifts of the readout cavity as well as its induced self-Kerr are negligible, which is confirmed by our experiments.

When no cat-quadrature readout drive is applied ( $\xi_{\text{eff},\text{cr}} = 0$ ) and the readout cavity is in the vacuum state (which is the case in our experiment whenever no readout is performed) equation (S6) simplifies to

$$\hat{H}_s/\hbar = \Delta_{as}\hat{a}^\dagger\hat{a} - K\hat{a}^{\dagger 2}\hat{a}^2 + \epsilon_2\hat{a}^{\dagger 2} + \epsilon_2^*\hat{a}^2 - 4K\hat{a}^\dagger\hat{a}|\xi_{\text{eff},s}|^2. \quad (\text{S7})$$

This implements the Hamiltonian (1) from the main text when we chose the frequency detuning  $\Delta_{as}$  such that it compensates for the Stark shift. In the experiment, this detuning can take on a more complicated form, because the pump-dependent frequency shift acquires additional contributions due to the single mode squeezing drive. Additionally, the Kerr-nonlinearity also acquires a perturbative second-order correction from the third-order nonlinearity [6]. For the data presented in Fig. 3 and Fig. 4 of the main text we perform a tuneup experiment (see section VIII) to eliminate all effective detunings. For the achieved squeezing-drive strength of  $\epsilon_2 = 17.75$  MHz we have to detune our drive by  $\Delta_{as} \approx 2.2$  MHz.

### III. ENERGY GAP AND SPECTRUM

In this section we give an estimate of the energy gap separating the states  $\{|\mathcal{C}_\alpha^+\rangle, |\mathcal{C}_\alpha^-\rangle\}$  from the rest of the energy spectrum of the ideal Hamiltonian (1) and compare the spectrum obtained from numerical diagonalization of the system Hamiltonian (S7) to experimental data.

To obtain an estimate of the gap we follow the derivation given in reference [1]. Applying a displacement transformation  $\hat{a} = \hat{a}' \pm \alpha$  to equation (1) and using  $\alpha = \sqrt{\epsilon_2/K}$  yields the Hamiltonian

$$\hat{H}'/\hbar = -4K\alpha^2\hat{a}'^\dagger\hat{a}' \mp 2\alpha K(\hat{a}'^\dagger\hat{a}' + \hat{a}'^\dagger\hat{a}'^2) - K\hat{a}'^\dagger\hat{a}'^2. \quad (\text{S8})$$

The vacuum state  $|0\rangle$  is an eigenstate of this Hamiltonian. In the non-displaced frame this corresponds to the states  $|\pm\alpha\rangle = D(\pm\alpha)|0\rangle$ , where  $D(\pm\alpha)$  is the displacement operator. In the limit of large  $\alpha$  this becomes the Hamiltonian of an effective harmonic oscillator of frequency  $-4K\alpha^2$ . Then the next-closest eigenstate is the Fock state  $|1\rangle$  which corresponds to a displaced state  $D(\pm\alpha)|1\rangle$  in the original frame. The energy gap is the energy difference between these states given by  $-4K\alpha^2 = -4K\bar{n}$ .

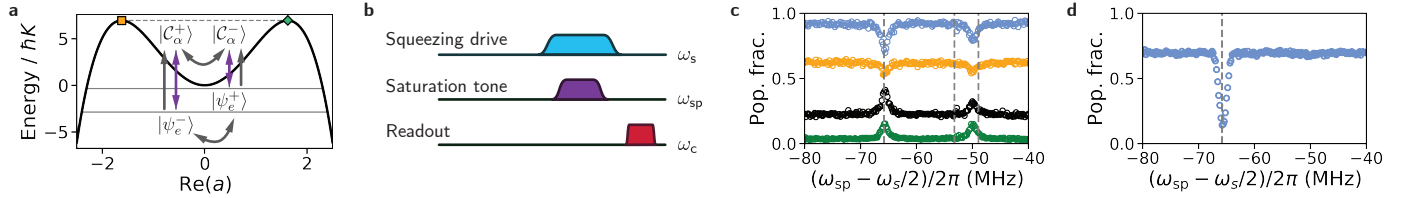


FIG. S1. **Kerr-cat qubit gap spectroscopy.** **a**, Solid black line: Energy dependence of equation (S7) on the classical phase space coordinate  $\text{Re}(a)$  for  $\text{Im}(a) = 0$ . Symbols indicate the coherent state amplitudes  $\pm\alpha$ . Gray lines are the result of the numerical diagonalization of the Hamiltonian. The dashed gray line marks the degenerate states  $|\mathcal{C}_\alpha^\pm\rangle$ . The two solid lines indicate the energies of the two closest eigenstates. Purple arrows symbolize the transitions due to the single photon drive, while gray arrows symbolize transitions due to photon loss. **b**, Pulse sequences for gap spectroscopy. The cat-qubit is initialized in  $|\mathcal{C}_\alpha^+\rangle$ . Then an saturation tone of varying frequency  $\omega_{\text{sp}}$  is applied followed by mapping back onto the Fock qubit and dispersive readout. **c**, Measured Population fraction of the Fock states  $|0\rangle$  (blue circles),  $|1\rangle$  (orange circles),  $|2\rangle$  (green circles),  $|n > 2\rangle$  (black circles) at the end of the experiment. The curves are offset for visibility. Gray dashed lines indicate the predicted transition frequencies (see text). The frequency axis is given with respect to the Stark-shifted mode frequency. **d**, Measured population fraction of the Fock state  $|0\rangle$  when instead of a saturation tone a short pulse is applied.

In our experiment we are not in the limit discussed above as  $\alpha \approx 1.6$ . In order to determine the energy spectrum we need to consider the full Hamiltonian (S7) using our system parameters given in section VII (we use the value  $\epsilon_2 \approx 17.75$  MHz). In Fig. S1a we plot its energy dependence on the classical phase space coordinate  $\text{Re}(a)$  for  $\text{Im}(a) = 0$  as a solid black line. This corresponds to a cut through Fig. 1c of the main text. We numerically diagonalize the Hamiltonian to obtain the energies of the degenerate states  $|\mathcal{C}_\alpha^\pm\rangle$  (dashed gray line in the figure) and of the closest two excited states  $|\psi_e^\pm\rangle \approx (D(\alpha) \pm D(-\alpha))|1\rangle$  (solid gray lines). The former can also be obtained from direct calculation by factorizing the Hamiltonian (1) [2]. We find that all states have well defined photon number parity (indicated by the  $\pm$  signs and that the energy differences between the cat-states and the states  $|\psi_e^\pm\rangle$  are  $-48.9 \text{ MHz} \times \hbar$  and  $-65.8 \text{ MHz} \times \hbar$  respectively. Note that while the wells in the figure are inverted in this frame, all dissipative processes bring the system from the states  $|\psi_e^\pm\rangle$  to the states  $|\mathcal{C}_\alpha^\pm\rangle$  [1].

We perform spectroscopy of the gap using the pulse sequence shown in Fig. S1b. First, we initialize the system in  $|\mathcal{C}_\alpha^+\rangle$  by ramping on the squeezing drive. Then, we apply a saturation tone of varying frequency  $\omega_{\text{sp}}$  and length  $20 \mu\text{s}$ . Finally, we map the system back onto the Fock qubit and perform dispersive readout. The latter can distinguish between the  $|0\rangle$ ,  $|1\rangle$ ,  $|2\rangle$  and  $|n > 2\rangle$  states of the Fock qubit. A coherent single photon drive does not conserve parity and thus we expect to drive the transitions  $|\mathcal{C}_\alpha^+\rangle \leftrightarrow |\psi_e^-\rangle$  and  $|\mathcal{C}_\alpha^-\rangle \leftrightarrow |\psi_e^+\rangle$  as indicated in Fig. S1a. At the same time, single photon loss also causes transitions between states of opposite parity as indicated in the figure by gray arrows. Since the mapping between the Fock-qubit and the cat-qubit Hamiltonian does conserve parity we expect the states  $|\psi_e^\pm\rangle$  to map onto the  $|2\rangle$  and  $|3\rangle$  states of the Fock qubit. The result of this experiment is shown in Fig. S1c. At several frequencies, we see a decrease in the population fractions of the  $|0\rangle$  and  $|1\rangle$  Fock states (blue and orange circles) and an increase in the population fractions of the  $|2\rangle$  and  $|n > 2\rangle$  Fock states (green and black circles). The two main peaks appear at  $-65.8 \text{ MHz}$  and  $-49.7 \text{ MHz}$  below the Stark-shifted mode frequency which are very close to the predicted values marked by dashed gray lines. An additional weak feature appears in both the  $|0\rangle$  and  $|n > 2\rangle$  curves at  $-52.9 \text{ MHz}$ . We interpret this as a two-photon transition from  $|\mathcal{C}_\alpha^+\rangle$  to another even parity state. Our numerical simulation indeed predicts such a state at an energy difference of  $-106.4 \text{ MHz} \times \hbar$  which corresponds to a two-photon

transition frequency of  $-53.2$  MHz (dashed gray line in the figure). Finally, we confirm the parity-dependent selection rule of the driven transitions by applying only a short pulse instead of a saturation tone. The corresponding data (see Fig. S1d) shows a marked dip in the  $|0\rangle$ -state population only at the frequency predicted for the transition  $|\mathcal{C}_\alpha^+\rangle \leftrightarrow |\psi_e^-\rangle$ , while as expected no response is observed for the transition  $|\mathcal{C}_\alpha^+\rangle \leftrightarrow |\psi_e^+\rangle$ .

#### IV. CONTINUOUS X-ROTATION

##### A. Adiabaticity of the X-rotation

To estimate the limit imposed on the continuous X-rotation we add a drive-term  $\epsilon_x \hat{a}'^\dagger + \epsilon_x^* \hat{a}'$  to the displaced ideal Hamiltonian (S8). Using the same approximation as in section III, the evolution of  $\hat{a}'$  is described by the quantum Langevin equation:

$$\partial_t \hat{a}' = 4iK\alpha^2 \hat{a}' - i\epsilon_x - \frac{\kappa_a}{2} \hat{a}' + \sqrt{\kappa_a} \hat{a}'_{\text{in}},$$

where  $\kappa_a/2\pi \approx 10$  kHz is the single-photon loss rate of the nonlinear resonator and  $\hat{a}'_{\text{in}}$  is the standard delta-correlated Gaussian vacuum noise with  $\langle \hat{a}'_{\text{in}} \rangle = 0$ . In the steady state, this translates to a displacement of the vacuum state by  $\alpha' = \langle \hat{a}' \rangle = \frac{\epsilon_x}{4K\alpha^2 + i\kappa_a/2}$ . In order for the gate to be adiabatic, such a displacement should not happen meaning that  $\pm\alpha$  are still the eigenstates of the Hamiltonian (1) in the original frame. This establishes a condition  $\epsilon_x \ll 4K\alpha^2$  for gate adiabaticity. In the work at hand, the maximum drive strength is approximately one order of magnitude weaker than the smaller of two gaps described in section III. Note also that the steady state is only reached after a ring-up time of  $1/\kappa_a = T_1 \approx 15.5$   $\mu\text{s}$ . The gate times presented in this work (on the order of  $\approx 10$  ns) are significantly shorter thus further relaxing the adiabaticity constraint. It is under this adiabaticity condition, and in the limit  $p \rightarrow 1$ , that the Rabi rate can be calculated by considering the energy difference of the states  $|\pm\alpha\rangle$  under the action of the  $\epsilon_x$  drive-term (yielding equation (2) of the main text). For small values of  $\alpha$  ( $p < 1$ , see section I), equation (2) is not a good estimate of the Rabi frequency as visible in Fig. 2b.

##### B. Numerical simulation

Here we describe the numerical simulation performed to obtain the results shown in Fig. 2. As discussed in sections II and VIII, we can compensate for all drive-related detunings by adjusting the drive frequencies. This is done for the data presented in Fig. 3 and Fig. 4. However, when measuring the data shown in Fig. 2 of the main text it would be impractical to perform this calibration for each drive strength  $\epsilon_2$ . Instead we apply the tone generating the squeezing drive at twice the unshifted mode frequency  $\omega_s = 2\omega_a$  and the X-rotation drive a frequency  $\omega_s/2$ . The resulting system Hamiltonian is

$$\hat{H}_s/\hbar = -K\hat{a}^{\dagger 2}\hat{a}^2 + \epsilon_2\hat{a}^{\dagger 2} + \epsilon_2^*\hat{a}^2 - 4K\hat{a}^\dagger\hat{a}|\xi_{\text{eff},s}|^2 + \epsilon_x\hat{a}^\dagger + \epsilon_x^*\hat{a}.$$

The third term (detuning due to Stark shift) results in smaller photon numbers  $\bar{n}$  than expected from equation (2) and we can thus not use the obtained Rabi frequency to directly calibrate  $\epsilon_2$ . Instead we fit a simulation of the above Hamiltonian including photon loss and gain (see section XI) to the Rabi oscillations obtained for the maximum drive strength shown in Fig. 2b with  $\epsilon_2$  as a free parameter. Our simulation mimics the experiment using the same initial state of the Fock qubit (4% thermal  $|1\rangle$ -state population) and rise times for the tanh-ramps of the squeezing drive (320 ns) and the X-rotation drive (80 ns) up to the point marked by a black arrow in Fig. 2a. At this point we compute  $\langle \mathcal{C}_\alpha^+ | \rho | \mathcal{C}_\alpha^+ \rangle$ , where  $\rho$  is the simulated density matrix of the non-linear resonator. In the experiment, the state  $|\mathcal{C}_\alpha^+\rangle$  is mapped onto the state  $|0\rangle$  of the Fock-qubit which is then measured. We scale the values obtained from simulation to match the readout contrast of the measured data.

#### V. CHARACTERIZATION OF GATE OPERATIONS

##### A. Process tomography

We perform process tomography on the different operations demonstrated in this work by making use of the mapping between the Fock qubit and the cat qubit. As described in the main text, for each operation, we initialize the cat-qubit in the states corresponding to each of the six cardinal points of its Bloch sphere by first applying the corresponding

pulses to the Fock qubit and then ramping on the squeezing drive. After the operation, we map the resulting state back onto the Fock qubit by ramping off the squeezing drive. We then apply one of three pulses (see Fig. 3) to the Fock qubit. The phase of these pulses is calibrated to correctly align the states on the equator of the Kerr-cat qubit and the Fock qubit. This is followed by dispersive readout. The entire sequence inside the gray box shown in Fig. 3a,c,e implements a measurement along each of the three axes of the Bloch sphere. Together with the six possible initial states this results in a total of 18 measured values.

In this process we make use of two properties of our system: First, the states  $|\mathcal{C}_\alpha^+\rangle$  and  $|\mathcal{C}_\alpha^-\rangle$  map back onto the  $|0\rangle$ - and  $|1\rangle$ -states of the Fock qubit, while other eigenstates of the Hamiltonian (S7) map onto higher-photon-number Fock states  $|n > 1\rangle$ . Second, the dispersive readout can distinguish between these three cases in a single shot. We calculate all 18 expectation values by taking the difference between the average thresholded  $|0\rangle$ - and  $|1\rangle$ -state populations. We normalize the obtained values using the difference of the average thresholded  $|0\rangle$ - and  $|1\rangle$ -state measurement contrast of Rabi oscillations on the Fock qubit. The sum of the the average thresholded  $|0\rangle$ - and  $|1\rangle$ -state populations is used to calculate the total population which corresponds to the expectation value of the identity (see next section). This value is normalized by the total averaged thresholded  $|0\rangle$ - and  $|1\rangle$ -state population of the same Rabi oscillations on the Fock qubit. This approach discards any population fraction that has potentially leaked outside of the encoding space spanned by  $\{|\mathcal{C}_\alpha^+\rangle, |\mathcal{C}_\alpha^-\rangle\}$  (e.g. to the states  $|\psi_e^\pm\rangle$ ) and thus takes into account this type of infidelity.

### B. Pauli-transfer-matrix method and fidelities

We characterize the fidelities of the performed gates including state-preparation and measurement errors with the Pauli-transfer-matrix (PTM) method described in references [8, 9]. To this end, we first reconstruct the experimental density matrix for each cardinal point by computing

$$\rho_i = \frac{1}{2}(\langle I \rangle_i \mathbb{1} + \langle X \rangle_i \sigma_x + \langle Y \rangle_i \sigma_y + \langle Z \rangle_i \sigma_z),$$

where  $\langle X \rangle_i, \langle Y \rangle_i, \langle Z \rangle_i$  and  $\langle I \rangle_i$  are the measured expectation values for a preparation on the cardinal point  $i \in \{\pm X, \pm Y, \pm Z\}$  and  $\mathbb{1}, \sigma_x, \sigma_y, \sigma_z$  are the identity and Pauli matrices. We do not perform maximum likelihood estimation or any other normalization on the computed density matrices in order to not discard potential infidelities due to leakage out of the encoding space.

Next, we express the experimental Pauli matrices (after application of the operation we wish to characterize) from the obtained density matrices as follows:

$$\begin{aligned} \mathbb{1}_{\text{exp}} &= \sum_i \rho_i / 3 \\ \sigma_{X,\text{exp}} &= \rho_{+X} - \rho_{-X} \\ \sigma_{Y,\text{exp}} &= \rho_{+Y} - \rho_{-Y} \\ \sigma_{Z,\text{exp}} &= \rho_{+Z} - \rho_{-Z} \end{aligned}$$

We can then calculate the  $4 \times 4$  Pauli transfer matrix fully characterizing of the operation with components

$$\mathcal{R}_{jk}^{\text{exp}} = \frac{1}{2} \text{Tr}(P_j^{\text{init.}} P_k^{\text{fin.}}),$$

where  $P_j^{\text{init.}}$  and  $P_k^{\text{fin.}}$  are the experimental Pauli matrices before and after the operation. We use the Pauli vector obtained for the mapping as  $P^{\text{init.}}$ . Finally, the fidelity  $\mathcal{F} = \frac{1}{3}(\frac{1}{2} \text{Tr}(\mathcal{R}^{\text{ideal},T} \mathcal{R}^{\text{exp}}) + 1)$  is calculated by comparing the obtained experimental Pauli transfer matrix  $\mathcal{R}^{\text{exp}}$  to the ideal one  $\mathcal{R}^{\text{ideal}}$ . We estimate the statistical error in fidelity with a bootstrapping approach by resampling each expectation value  $10^4$  times from a Gaussian distribution with a width given by the standard measurement error which is  $< 0.006$  for all measured expectation values. The experimental and ideal PTMs for the operations presented in the main text are shown in Fig. S2. The associated fidelities are summarized in table S1.

### C. Additional gate characterization

The PTM estimate of the X-gate fidelity described above is mostly limited by state preparation and measurement errors as evidenced by the fact that its value is the same as the mapping fidelity (within error bars). To further

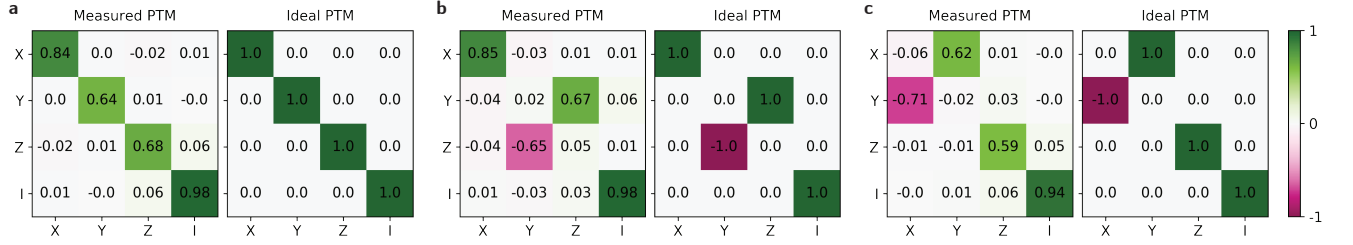


FIG. S2. **Pauli transfer matrix.** **a,b,c**, Measured ( $\mathcal{R}^{\text{exp}}$ ) and ideal ( $\mathcal{R}^{\text{ideal}}$ ) Pauli-transfer-matrix (PTM) representations of the mapping operation, the  $X(\pi/2)$  rotation, and the  $Z(\pi/2)$  rotation respectively. The three datasets correspond to the Bloch-sphere representations shown in Fig. 3b, d, and f of the main text.

Operation	Fidelity (%)	Error $\pm 3\sigma$ (%)
Mapping	85.5	$\pm 0.5$
$X(\pi/2)$	85.7	$\pm 0.4$
$Z(\pi/2)$	81.1	$\pm 0.4$

TABLE S1. **Fidelities and statistical errors**, Fidelities are computed using the Pauli-transfer-matrix approach described in the text. The errors are estimated using a bootstrap method.

investigate the quality of the  $X(\theta)$  gate, we perform an additional characterization experiment. As depicted in the pulse sequence of Fig. S3a, we initialize the cat-qubit in  $|\mathcal{C}_\alpha^+\rangle$ , play a randomly generated sequence of  $n$  gates uniformly selected from  $\{X(\pi/2), X(\pi)\}$ , play an undo pulse that would set the cat-qubit back to  $|\mathcal{C}_\alpha^+\rangle$  if all gates were perfect, ramp back down to the Fock-qubit and perform a symmetrized dispersive readout. The dependence of the ensemble-averaged  $\langle Z \rangle$  on the length of the random sequence  $n$  is shown in Fig. S3b. We fit the data with a single-exponential with decay constant  $\tau_n = 35.7$ . The gate error for the  $X(\theta)$  gate is then estimated via  $r = (1 - e^{-n/\tau_n})/2 = 0.014$ , and the fidelity is  $\mathcal{F}_X = 1 - r = 98.6$ . The measured fidelity includes over-rotations, leakage out of the cat-encoding space and decoherence. Note that we estimate the probability for a bitflip to occur during the gate operation to be  $T_{X(\theta)}/\tau_{+Y} \approx 0.01$ .

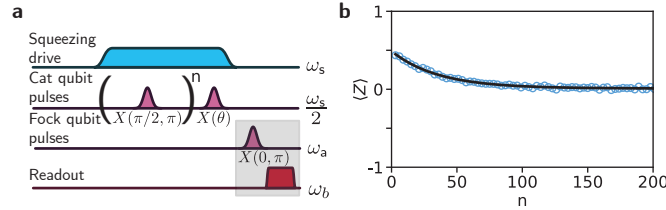


FIG. S3. **Additional gate characterization** **a**, Pulse sequence to perform the following functions: (i) initialize the Kerr-cat-qubit in  $|\mathcal{C}_\alpha^+\rangle$ , (ii) perform random sequence of  $n$  gates (here either  $X(\pi/2)$  or  $X(\pi)$ ), (iii) perform an undo gate  $X(\theta)$  where  $\theta$  is calculated to map the state back to  $|\mathcal{C}_\alpha^+\rangle$ , (iv) map onto the Fock qubit and perform symmetrized dispersive readout (grey box). **b**, Dependence of  $\langle Z \rangle$  on the number of random gates applied  $n$ , where the average is an ensemble average over random sequences. Open blue circles are data and solid black line is a single exponential fit (see text).

## VI. EXPERIMENTAL SETUP

### A. System details and sample design

As described in the main text, our system includes a nonlinear resonator (see Fig. 1e), which hosts the quantum information, and a copper/aluminum readout cavity. The former consists of a nonlinear inductance given by a superconducting asymmetric nonlinear element (SNAIL) which is shunted by a large capacitance coming from the two pads of dimension  $2.2 \text{ mm} \times 0.6 \text{ mm}$  visible in the photograph of Fig. 1d. The SNAIL is a superconducting ring, placing a small Josephson junction (inductance  $7.27 \text{ nH}$ ) in parallel with three large junctions (inductance  $0.8 \text{ nH}$  per junction). The inductance values are estimated from room-temperature measurements of nominally identical test junctions on the same chip. This element has flux-tunable third- and fourth-order nonlinearities. We employ it here because it

allows us to dissociate the strength of the single mode squeezing drive  $\epsilon_2 = 3g_3\xi_{\text{eff},s}$  from the Kerr-nonlinearity  $K$  (see section II). This makes it possible to stabilize cats with appreciable photon numbers  $\bar{n} = \epsilon_2/K$  while limiting unwanted heating effects due to excessively strong drives amplitudes  $\xi_{\text{eff},s}$  [10]. While the large capacitor pads are necessary to reduce the Kerr nonlinearity of the resonator, they lead to a large electric dipole moment. Strong coupling between the resonator and the readout cavity is not desirable for this experiment and so we avoid this by orienting the resonator perpendicularly to the electrical field direction of the lowest frequency cavity mode. In order to reintroduce a small cross-Kerr  $\chi_{ab}$ , which is necessary for dispersive readout, we offset the capacitor pads by  $\delta = 0.22$  mm. The next higher frequency mode has a field node at the position of the resonator and does not couple significantly to it. Higher frequency modes are far enough detuned to be negligible.

The readout cavity has two halves. Only the lower half is shown in Fig. 1d. It is made from copper to let in the magnetic field used to tune the nonlinear resonator. The upper half is made from aluminum and is coupled to an aluminum WR-90 waveguide through an aperture. The waveguide itself couples to a transmission line through a  $50\ \Omega$ -matched pin. It acts as a high-pass Purcell filter with a cutoff frequency of  $\approx 8.2$  GHz. This limits the decay of the nonlinear resonator into the continuum of modes of the transmission line, while letting pass the readout signal at frequency 8.9 GHz and the tone at  $\approx 12$  GHz which generates the squeezing drive. The cavity additionally has a weakly coupled port realized with a standard coupling pin which allows us to drive the nonlinear resonator at  $\approx 6$  GHz and apply the conversion drive at  $\approx 2.9$  GHz used for cat-quadrature readout. Both coupling-strengths are calibrated and tuned at room temperature using vector network analyzer transmission and reflection measurements. The entire system is shielded by both an aluminum- and a cryoperm-enclosure and thermalized to the base-stage of a dilution refrigerator at a temperature of  $\approx 18$  mK as indicated in Fig. S4.

When designing the system we simulate its parameters in an iterative process. We first use a 3D electromagnetic field simulation software (ANSYS HFSS) and the black-box circuit quantization formalism [11] to predict the charging energy of the nonlinear resonator and its coupling strength to the cavity for the effective inductance of the SNAIL-element at a given flux point. Next, we calculate the resulting circuit parameters  $g_3, K, \omega_a, \omega_b$  and the effective cross-Kerr  $\chi_{ab}$  with a homemade program following the method described in reference [6, 12]. We then feed back onto the dimensions of the resonator and the inductances of the Josephson junctions until we achieve the desired parameters.

## B. Wiring diagram

The wiring diagram shown in Fig. S4 has seven branches which are numbered at the boundary with the dilution refrigerator in the schematic. From left to right in the figure they are: 1) the DC-current line used to generate an external magnetic field for the flux bias of the SNAIL, 2) the RF-line for the Josephson parametric converter (JPC) amplifier pump tone, 3) the readout output line, 4) the readout input line ( $\omega_b$ ), 5) the line delivering the tone at frequency  $\approx 2\omega_a$  which generates the squeezing drive, 6) the line delivering the tone at frequency  $\omega_{\text{cr}}$  generating the interaction for cat-quadrature readout, and 7) the line used to resonantly address the nonlinear resonator at frequency  $\approx \omega_a$ .

The DC-line 1) connects a current source at room-temperature via a twisted-pair cable (normal metal from 300 K to 4 K, superconducting below) to a superconducting magnet spool. This is used to thread a flux through the loop of the SNAIL element.

The next three lines 2) - 4) constitute a standard single-shot readout setup for a superconducting circuit experiment. A resonant tone (applied on line 4) is reflected of the readout cavity and acquires a qubit-state dependent phase shift. It is then routed to a JPC (which has a separate pump line numbered 2), reflected off with gain, routed to the output (line 3) and digitized after further amplification at 4 K and room temperature using an analog-to-digital converter (ADC). Two power splitters allow us to directly perform measurements with a vector network analyzer (VNA) for tuneup and characterization. When performing cat-quadrature readout, the same setup is used, but no drive is applied on line 4), because the readout signal is generated directly at the sample (see section IX).

The last three lines 5) - 7) deliver the essential drives of the experiment. These drives need to have high phase-stability with respect to each other and are thus created by mixing together the tones coming from two generators one of which (marked “Readout generator”) is set to a frequency  $\omega_b/2\pi + 50$  MHz while the other (marked “Qubit generator”) is set to  $\omega_a/2\pi + 40$  MHz. Each branch going into the dilution refrigerator includes an IQ-mixer which takes its I and Q inputs from an FPGA-based DAC equipped with homemade software. These mixers modulate the the high-frequency tones with slow-varying envelopes ( $\epsilon_{\text{cr}}, \epsilon_s$ ) and are calibrated such that they give out a single sideband at the respective desired frequency. The DAC has a sampling rate of  $\approx 500$  MHz and is filtered with a low-pass filter at  $\approx 250$  MHz to avoid aliasing. This limits the rise-time of the step-function used to perform the  $Z(\pi/2)$ -gate shown in Fig. 2f to  $\approx 4$  ns and allows us to create sidebands at a frequency difference of  $\approx \pm 125$  MHz from the carrier tone.



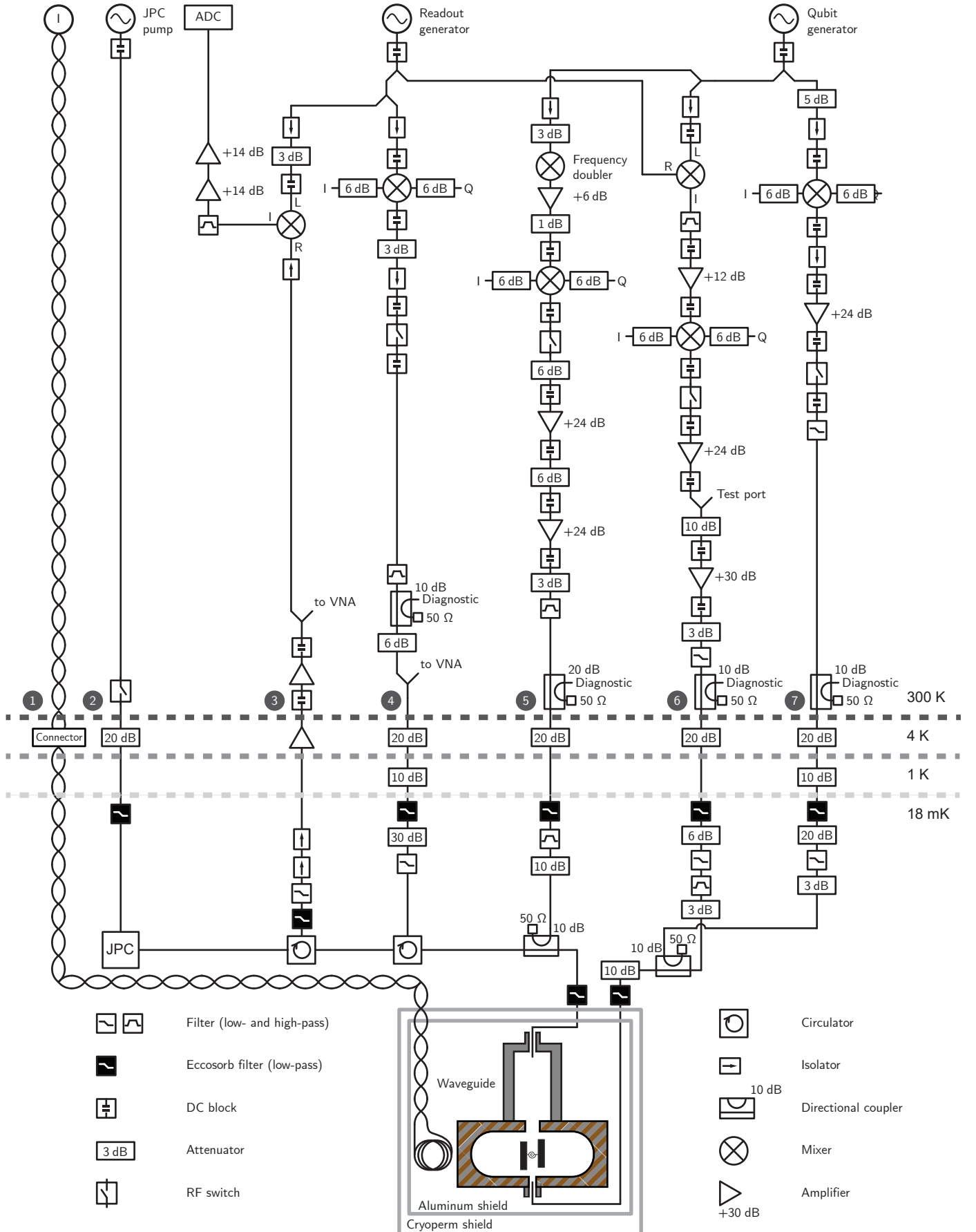


FIG. S4. **Wiring diagram**, A legend for the main elements is given. Attenuation or gain is indicated in dB where relevant. The different relevant temperature stages are indicated on the right-hand side. The sketch of the sample shows the nonlinear resonator inside the copper/aluminum readout cavity (brown/gray hashed) which is aperture-coupled to a waveguide. See text for description.

We now describe these three lines in turn: Line 5) uses an amplifying frequency doubler (shown as two elements in the figure) to generate a tone at  $2\omega_a/2\pi + 80\text{ MHz}$  which is then modulated and converted to the frequency  $\omega_s/2\pi \approx 2\omega_a/2\pi$ . We use isolators and attenuators in order to suppress reflections and leakage of reflected tones to other branches. The losses introduced by these elements as well as the mixers are counterbalanced by adding several amplifiers to the branch which are chosen such that the maximum amplitude of the mixer output leads to an output power on the last amplifier just below its 1 dB compression point (although the power used in the final experiment presented here is  $< 10\%$  of this maximum power). A switch helps to suppress the carrier leakage of the IQ-mixer when no drive is applied and a bandpass filter at the input of the dilution refrigerator is chosen such that it strongly suppresses the noise generated by this chain at all relevant mode frequencies of the experiment. Note that, because of the third-order nonlinear process used here, the frequency of the drive is far off-resonant from  $\omega_a$  and  $\omega_b$  making this approach possible. Just before the line enters the dilution refrigerator (DR) a directional coupler reroutes a fraction of the signal to dedicated spectrum analyzer for diagnostic and mixer tuneup. Further attenuation and filtering inside the DR is followed by a directional coupler which we use here as a broadband combiner to merge this line with the readout tone before entering the waveguide.

Line 6) is laid out according to similar principles as line 5). The carrier is generated by mixing the frequencies of the readout generator and the qubit generator to give  $\omega_b/2\pi - \omega_a/2\pi + 10\text{ MHz}$  which is modulated by the IQ-mixer to give  $\omega_{\text{cr}}/2\pi$ . The resulting drive is sent into the weakly coupled port of the system. The filters on this line are either low-pass with a cutoff frequency between  $\omega_{\text{cr}}/2\pi$  and  $\omega_a/2\pi$  or band-pass centered around  $\omega_{\text{cr}}/2\pi$ .

The last line to be described here is branch 7) which is used both to resonantly address the Fock qubit as well as the Kerr-cat qubit when necessary (e.g. for the X-rotation described in the main text) following again similar principles as before. The filters on this line are low-pass with a cutoff situated between the frequencies of the nonlinear resonator and the readout cavity.

## VII. SYSTEM PARAMETERS

Parameter	Value	Method of estimate or measurement
Nonlinear resonator frequency $\omega_a/2\pi$	6 GHz	Two-tone spectroscopy
Readout cavity frequency $\omega_b/2\pi$	8.9 GHz	Direct RF reflection msmt.
Nonlinear resonator single-photon decay time $T_1$	15.5 $\mu\text{s}$	Std. coherence msmt.
Nonlinear resonator transverse relaxation time $T_2$	3.4 $\mu\text{s}$	Std. Ramsey coherence msmt.
Nonlinear resonator transverse relaxation time (echo) $T_{2e}$	13.7 $\mu\text{s}$	Std. Ramsey echo coherence msmt.
Readout cavity linewidth (output coupling) $\kappa_{b,c}/2\pi$	1.4 MHz	Direct RF reflection msmt.
Readout cavity linewidth (other losses) $\kappa_{b,l}/2\pi$	0.5 MHz	Direct RF reflection msmt.
Kerr-nonlinearity $K/2\pi$	6.7 MHz	Saturation spectro. of $ 0\rangle \leftrightarrow  2\rangle$ transition
Third-order nonlinearity $g_3/2\pi$	$\approx 20\text{ MHz}$	Design simulation, fit of tuneup
Cross-Kerr $\chi_{ab}/2\pi$	$\approx 200\text{ kHz} - 250\text{ kHz}$	Design simulation, and msmt. ind. deph. [13]
Cat-Rabi-drive strength $\epsilon_x/2\pi$ (Fig. 2)	740 kHz	From Fock-qubit Rabi frequency
Cat-Rabi-drive strength $\epsilon_x/2\pi$ (Fig. 3, Fig. 4)	6.5 MHz	Extrapolated from above
Squeezing-drive strength $\epsilon_2/2\pi$ (Fig. 2)	15.5 MHz	Fit to simulation (section IV B)
Squeezing-drive strength $\epsilon_2/2\pi$ (Fig. 3, Fig. 4)	17.5 MHz-18 MHz	From equation (2), extrapolated from above
Detuning to compensate Stark shifts $\Delta_{as}/2\pi$	2.2 MHz	Tuneup experiment (section VIII)
Frequency-conversion interaction strength $g_{\text{cr}}/2\pi$	1.7 MHz	Fock-qubit decay under driving (section IX)

TABLE S2. **System parameters.** Summary of the main system parameters discussed in the main text and section II with a short summary of how they are measured or estimated. More details and additional parameters are given in the text. Bolder horizontal lines separate from top to bottom: system frequencies, coherence parameters, nonlinearities, and parameters of the system under driving.

In this section we give the parameters of our system as summarized in Table S2. All parameters are given for the flux-bias used for all experiments presented in this work corresponding to a flux through the SNAIL loop of  $\Phi \approx 0.26\Phi_0$ , where  $\Phi_0 = h/2e$  is the superconducting magnetic flux quantum. We calibrate the flux-bias from a multi-period sweep of the small inherited flux-dependence of the readout-cavity frequency.

The coherence times of the nonlinear resonator (i.e. the Fock qubit) are measured using standard experiments. The values presented in the table were obtained during the same cooldown as the data presented in the rest of this work. Over several cooldowns we observe variations of  $\approx \pm 3\mu\text{s}$  on the single-photon decay time and  $\approx \pm 1\mu\text{s}$  on the transverse relaxation time for comparable flux-biases. In general, the latter time becomes shorter when tuning to flux-bias values where  $\partial\omega_a/\partial\Phi$  increases indicating that it is limited by flux-noise.

We extract the total cavity linewidth at base temperature by performing a reflection measurement of the resonator response and fitting the resulting circle in the complex plane. This yields the part of the linewidth coming from the coupling to the waveguide  $\kappa_{b,c}/2\pi = 1.4$  MHz and the part due to other losses  $\kappa_{b,l}/2\pi = 0.5$  MHz. From room-temperature calibration we estimate that the weakly coupled pin accounts for  $\approx 80$  kHz of the latter number.

The Kerr-nonlinearity is measured by applying a strong saturation tone of varying frequency  $\omega_{\text{sat}}$  to the nonlinear resonator and measuring its response with dispersive readout. At a detuning of  $\omega_a - \omega_{\text{sat}} = K$  this tone excites the two-photon transition  $|0\rangle \leftrightarrow |2\rangle$  which allows us to determine the value of  $K$ .

We estimate the value of the third-order nonlinearity from our design simulation to lie between 15 MHz and 30 MHz. The large margin in this estimate comes from the fact that the linear inductance of the leads between the SNAIL element and the capacitive pads is only roughly estimated in the simulation. We estimate the experimental value of  $g_3$  by reproducing the tuneup-experiment described in section VIII in simulation (using equation (S7)). We fix all parameters including  $\epsilon_2 = 3g_3\xi_{\text{eff},s}$  and vary  $g_3$  until the effective Stark shift matches the detuning  $\Delta_{as}$  such that we observe no spurious Z-rotation. This procedure yields a value of  $g_3/2\pi \approx 20$  MHz and is sensitive to variations in this estimate on the order of  $\approx \pm 1$  MHz. This also lets us estimate the dimensionless pump strength used in the experiment as  $\xi_{\text{eff},s} \approx 0.29$ .

The estimate of the cross-Kerr term based on our design simulation is  $\chi_{ab}/2\pi \approx 250$  kHz. We verify this estimate by conducting a Ramsey experiment on the Fock qubit in the presence of a drive on the readout cavity. From the change in transverse relaxation time and oscillation frequency of the Ramsey curve we infer the effective cross-Kerr as described in reference [13]. This experiment is performed for a single drive-power giving a rough estimate of the cross-Kerr which we round to the leading digit  $\chi_{ab} \approx 200$  kHz. This also allows us to estimate  $g/\Delta \approx 0.1$  used in section II.

The drive strength  $\epsilon_x$  for the data presented in Fig. 2 is measured directly from the Rabi-frequency of the Fock qubit  $\Omega_f = 2\epsilon_x$  when no squeezing drive is applied. The strength of the drive applied to perform the  $X(\pi/2)$ -rotation presented in Fig. 3 is obtained from a linear extrapolation of this value using the known mixer-amplitudes for both cases.

The value of  $\epsilon_2/2\pi = 15.5$  MHz for the measurements presented in Fig. 2 of the main text is extracted from simulation as described in section IV B. In this case, we cannot use the formula  $\epsilon_2 = K\bar{n}$  together with the photon-number calibration given by the Rabi-frequency of the cat qubit (see equation (2)), because the uncompensated Stark shifts reduce the photon number  $\bar{n} = 2.2$ . In the case where we compensate for the Stark shifts (i.e. Fig. 3 and Fig. 4), we can directly calculate the squeezing drive strength  $\epsilon_2/2\pi \approx 17.5$  MHz from these expressions. Extrapolating the drive strength found for Fig. 2, yields a similar value of  $\epsilon_2/2\pi \approx 18$  MHz.

The detuning  $\Delta_{as}/2\pi = 2.2$  MHz is calibrated as described in section VIII. The coupling strength of the frequency-converting interaction used for cat-quadrature readout  $g_{\text{cr}}$  is measured as described in section IX. The remaining Hamiltonian parameter  $\xi_{\text{eff},\text{cr}} \approx 0.15$  is not directly measured but estimated using the expression for  $g_{\text{cr}}$ .

The thermal photon number of the nonlinear resonator  $n_{\text{th}} = 0.04$  is determined with the Rabi population measurement method described in reference [14].

## VIII. TUNEUP SEQUENCE

In this section, we describe the key tuneup experiments employed to generate a cat-qubit with a specific photon number  $\bar{n} = |\alpha|^2$  and calibrate the phases of the different RF drives to account for line dispersion and Stark shifts as seen in (S7). The effect of Stark shifts can be described by considering the effect of a Hamiltonian term  $\Delta\hat{a}^\dagger\hat{a}$  where  $\Delta = \Delta_{as} - 4K|\xi_{\text{eff},s}|^2$  and  $\Delta_{as} = \omega_a - \omega_s/2$ . Projected in the cat-qubit basis, this Hamiltonian reduces to  $\Omega_z\hat{\sigma}_z$  where the Rabi rate around the Z-axis is  $\Omega_z = -4\Delta|\alpha|^2e^{-2|\alpha|^2}$  [2]. We use this effect in experiment to tune  $\omega_s$  to minimize  $\Omega_z$  for a given drive strength.

The work flow is as follows: We choose a given frequency  $\omega_s$  and drive strength for the drive used to generate the squeezing. We perform an experiment identical to the phase-dependant time-Rabi experiment in Fig. 2c to calibrate the phase of  $\epsilon_x$ , which depends on the relative line dispersion between the qubit-drive and squeezing-drive lines, and measure  $\Omega_x$  to extract  $\bar{n}$  for these stabilization-drive parameters. Next, we calibrate the relative phase between the Fock-qubit pulses at  $\omega_a$  and the cat-qubit at  $\omega_s/2$  so that preparing  $|+X\rangle$  on the Fock qubit and performing the adiabatic ramp up of  $\epsilon_2$  maps to  $|+X\rangle$  of the cat qubit. The pulse sequence used for this calibration is given in Fig. S5a: prepare  $|+X\rangle$  on the Fock qubit, adiabatically ramp to the cat-qubit, apply Rabi drive  $\epsilon_x$  with the previously calibrated phase for a varying time  $\Delta t$ , map back onto the Fock qubit and perform dispersive readout. We sweep the squeezing-drive phase  $\arg(\epsilon_2)$  and the Rabi phase  $\arg(\epsilon_x)$  together, maintaining the calibrated difference between them, and plot the resulting dependence of the Rabi oscillations in Fig. S5b. The phase for which Rabi oscillations are suppressed (white horizontal lines) marks the phase for which the cat-qubit state was  $|+X\rangle = |\alpha\rangle$ ,

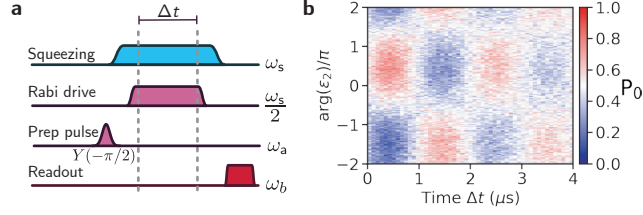


FIG. S5. **Stabilization-drive phase tuneup** **a**, Pulse sequence to perform the following functions: (i) initialize the Kerr-cat-qubit on the equator of the Bloch sphere, (ii) drive Rabi oscillations for a varying time  $\Delta t$ , (iii) map onto the Fock qubit and perform dispersive readout. **b**, Dependence of Rabi oscillations on time  $\Delta t$  and on the stabilization drive phase  $\arg(\epsilon_2)$ . The color scale gives the ground state population of the Fock qubit ( $P_0$ ) at the end of the sequence.

thus calibrating our mapping between the Fock and cat qubits. Note that the data are  $4\pi$  periodic in the squeezing-drive phase  $\arg \epsilon_2$ , which is a result of the period-doubling phenomenon since there are two valid values of  $\alpha$  in the frame rotating at  $\omega_s/2$ . For poor combinations of stabilization drive amplitude and frequency, the white lines in the data would be tilted due to the spurious Z-rotation at rate  $\Omega_z$ . This tuneup procedure can be iterated to minimize the measured  $\Omega_z$  by choosing a new squeezing drive frequency or new  $\epsilon_2$ . The end result is a set of squeezing- and Rabi-drive parameters for a given cat-qubit of size  $\bar{n}$  and the ability to prepare any point on the cat-qubit Bloch sphere through preparation of the Fock qubit and adiabatic mapping.

Finally, we discuss how to tune up the gates. For the  $X(\theta)$  gate, a standard amplitude-Rabi experiment is performed where the qubit is prepared in  $|\mathcal{C}_\alpha^+\rangle$ , a Gaussian pulse at  $\omega_s/2$  of variable amplitude with the calibrated phase is applied, and Rabi oscillations are observed through mapping back to the Fock qubit and performing dispersive readout. This easily calibrates the pulse amplitude for a desired  $\theta$ . For the  $Z(\pi/2)$  gate, we turn the stabilization drive off for  $T_{Z(\pi/2)} = 38 \text{ ns} \approx \pi/2K$ . The free Kerr evolution under  $-K\hat{a}^{\dagger 2}\hat{a}$  for  $\pi/2K$  takes for example  $|-Y\rangle = |\mathcal{C}_\alpha^{+i}\rangle \rightarrow |\alpha e^{i\varphi}\rangle$  with  $\varphi = -\pi/2 + \Delta_{as}T_{Z(\pi/2)}$  where the first term comes from the free Hamiltonian and the second comes from the absence of Stark shift while the stabilization drive is off. As such, when switching the stabilization drive back on, we boost it in phase by  $2\varphi$  and redefine the cat-qubit frame such that  $|+X\rangle = |\alpha e^{i\varphi}\rangle$ . All future  $X(\theta)$  gate pulses and all future Fock qubit pulses are also boosted by phase  $\varphi$ . In experiment, we optimize  $\varphi$  to maximize the  $Z(\pi/2)$  gate fidelity, but the calibrated value almost identically aligns to the above calculation.

## IX. CAT-QUADRATURE READOUT

### A. Parametric process

In this section, we derive how adding a drive at  $\omega_{\text{cr}} = \omega_b - \omega_s/2$ , while the squeezing drive is on, implements the quantum non-demolition (QND) cat-quadrature readout. The parametric process generated by this drive displaces the readout cavity (annihilation operator  $\hat{b}$ ) conditioned on the  $\hat{\sigma}_x$  state of the qubit. To see this, we derive the interaction Hamiltonian in the cat-qubit basis and solve the resulting dynamics of the readout cavity. Starting from equation (3), we express  $\hat{a}$  in the cat-qubit basis (see section I) and write the Hamiltonian projected on the cat-qubit Bloch sphere as:

$$\hat{H}_{\text{cr}}/\hbar = ig_{\text{cr}}\alpha \left( \frac{p+p^{-1}}{2} \right) (\hat{b}^\dagger - \hat{b})\hat{\sigma}_x - g_{\text{cr}}\alpha \left( \frac{p-p^{-1}}{2} \right) (\hat{b}^\dagger + \hat{b})\hat{\sigma}_y \quad (\text{S9})$$

$$\approx ig_{\text{cr}}\alpha (\hat{b}^\dagger - \hat{b})\hat{\sigma}_x \quad (\text{S10})$$

where  $g$  is proportional to the drive amplitude at  $\omega_{\text{cr}}$ , and in the second line we have used  $p \approx 1$  for modest  $\bar{n}$  (see section I) or equivalently that  $|\pm X\rangle \approx |\pm \alpha\rangle$ . Using this Hamiltonian, we describe the dynamics of  $\hat{b}$  with the quantum Langevin equation:

$$\partial_t \hat{b} = \frac{i}{\hbar} [\hat{H}_{\text{cr}}, \hat{b}] - \frac{\kappa_b}{2} \hat{b} + \sqrt{\kappa_b} \hat{b}_{\text{in}} \quad (\text{S11})$$

$$\approx g_{\text{cr}}\alpha \hat{\sigma}_x - \frac{\kappa_b}{2} \hat{b} + \sqrt{\kappa_b} \hat{b}_{\text{in}} \quad (\text{S12})$$

where  $\kappa_b/2\pi = 1.9 \text{ MHz}$  is the total linewidth of the readout cavity, and  $\hat{b}_{\text{in}}$  is the standard delta-correlated input field with the property  $\langle \hat{b}_{\text{in}} \rangle = 0$  since we apply no drives at  $\omega_b$  for this readout. In a semi-classical treatment, we

then solve for the coherent-state amplitude  $\beta = \langle \hat{b} \rangle$  in response to turning on  $\omega_{\text{cr}}$  at time  $t = 0$  giving

$$\beta(t, \sigma_x) = \frac{2g_{\text{cr}}\alpha}{\kappa_b} \sigma_x \left[ 1 - e^{-\kappa_b t/2} \right] \quad (\text{S13})$$

where  $\sigma_x = \pm 1$  encodes the two possible measured qubit states. The steady state value is therefore  $|\beta\rangle$  with  $\beta = \pm 2\alpha g_{\text{cr}}/\kappa_b$ . We can use this steady state  $\beta$  to estimate the validity of our projection into the cat-qubit manifold. In a mean-field treatment, we take  $\hat{b} \rightarrow \beta$  in (3) resulting in a Hamiltonian that implements a single-photon drive on the cat mode of the form  $-ig_{\text{cr}}\beta(\hat{a}^\dagger - \hat{a})$ . Out-of-manifold leakage caused by this drive is suppressed so long as  $|g_{\text{cr}}\beta| \ll E_{\text{gap}}/\hbar$ ; the same condition for suppressed leakage in the  $X(\theta)$  Rabi gate. Moreover, this drive has a  $\pi/2$  phase shift with respect to the optimal drive phase  $\arg(\epsilon_x)$  and therefore does not generate spurious in-manifold rotations.

## B. Strength of coupling

Here, we independently measure the induced coupling strength  $g_{\text{cr}}$  in (3). As can be seen in the pulse sequence of Fig. S6a, we perform a  $T_1$  measurement of the Fock qubit while turning the frequency-conversion drive on during the wait time. For  $g_{\text{cr}} \ll \kappa_b$ , the coupling to the readout cavity enhances the effective damping rate on the qubit and thus reduces the measured  $T_{1\text{eff}}$  to  $1/T_{1\text{eff}} = 1/T_1 + 4g_{\text{cr}}^2/\kappa_b$ . This is often termed “Q-switch” and is commonly used for cooling. In our case, since  $g_{\text{cr}} \approx \kappa_b$ , we are actually driving Rabi oscillations between the bare Fock qubit and the readout cavity, which then leak out of the cavity at rate  $\kappa_b$ , see Fig. S6b. Following the supplement of Ref. [15], we start from (3) write the equations of motion for  $\hat{a}$ . We then solve the dynamics with the initial conditions of  $\hat{a}(0)$  for the qubit and with the readout cavity in vacuum to get:

$$\hat{a}(t) = \frac{\hat{a}(0)}{\Omega} e^{-\kappa_b t/4} \left( \Omega \cosh \frac{\Omega t}{4} + \kappa_b \sinh \frac{\Omega t}{4} \right) \quad (\text{S14})$$

where  $\Omega = \sqrt{\kappa_b^2 - (4g_{\text{cr}})^2}$  is in general complex. Here we have assumed that the quadrature readout drive is on-resonance at  $\omega_{\text{cr}} = \omega_b - \omega_a$ . In practice, the Fock-qubit frequency is Stark-shifted by the quadrature readout drive (see Eq. S7), but we find the induced Stark shift  $4K|\xi_{\text{eff,cr}}|^2 < \kappa_b$  to be small for our drive strength. In the experiment, we extract the Fock qubit population with dispersive readout, so we measure  $\langle \hat{n}(t) \rangle = \langle \hat{a}^\dagger(t)\hat{a}(t) \rangle$ . We fit the data with the corresponding expression resulting from equation S14 with the initial condition  $\langle \hat{n}(0) \rangle = 1$ . Together with a scaling factor and an offset to compensate for readout contrast, we extract the only other free parameter  $g_{\text{cr}}/2\pi = 1.7$  MHz.

Importantly, as noted in the analysis in the previous section, despite  $g \approx \kappa_b$ , such Rabi oscillations do not occur when the squeezing drive is on and the cat-quadrature readout is performed. Intuitively, because  $|g_{\text{cr}}\beta| \ll E_{\text{gap}}/\hbar$ , the squeezing drive replenishes any photon that leaves the Kerr-cat mode before one Rabi-oscillation cycle can be completed. Further excitation of the Kerr-cat mode is then suppressed by the stabilization.

## C. Signal treatment

Here, we briefly describe the signal treatment to generate histograms for the cat-quadrature readout and assign a binary value based on a threshold for single-shot measurements. These procedures are nearly identical to those performed for dispersive readout. To generate the histograms shown in Fig. 4a, the full time trajectory of the readout signal associated with signal  $\hat{b}_{\text{out}} = \sqrt{\kappa_b}\hat{b} - \hat{b}_{\text{in}}$  is recorded via heterodyne detection (50 MHz intermediate frequency) and digitized for each cat-qubit preparation  $|\pm\alpha\rangle$ . We denote the average over many experimental shots of these two trajectories as  $\beta_{\text{out}}^\pm(t)$ . For each shot  $m$ , we assign a point on the IQ-plane  $(I_m, Q_m)$  by integrating the measured signal over the full measurement time  $\tau$  as:  $\int_0^\tau [\hat{b}_{\text{out}} e^{-i\varphi} + \hat{b}_{\text{out}}^\dagger e^{i\varphi}] K(t) dt$  where  $\varphi = (0, \pi/2)$  for  $(I_m, Q_m)$  and  $K(t)$  is the integration envelope. We use the envelope  $K(t) = (\beta_{\text{out}}^+ - \beta_{\text{out}}^-)^*$  [16] to assign  $(I_m, Q_m)$  and generate the histogram. We also offset the I and Q axes by a small independently measured amount coming from leakage inside our interferometer. This offset is however negligible compared to the width of the histograms and is only necessary to confirm that  $|\pm\alpha\rangle$  indeed generate equal and opposite displacements on the readout cavity.

To calibrate a single-shot thresholded measurement, we integrate over the Q-axis resulting in the histograms shown in the bottom panel of Fig. 4a. We fit each histogram to a Gaussian and scale the I-axis by the resulting width  $\sigma$  (same for both  $|\pm\alpha\rangle$ ). The mean between the two centers of the Gaussians is exactly  $I = 0$ , where we then set our threshold for state assignment of future single-shot measurements.

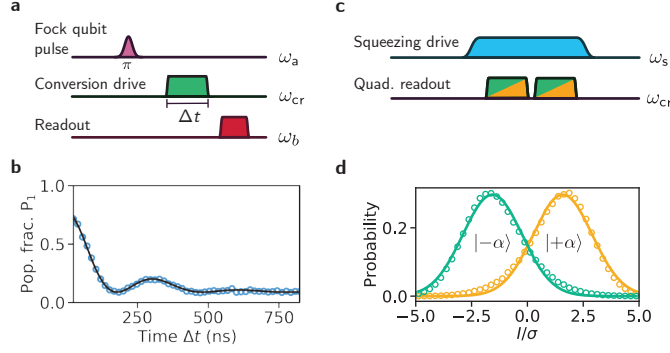


FIG. S6. **Readout strength and QND-ness** **a**, Pulse sequence to measure the coupling strength  $g_{cr}$ . A  $\pi$  pulse prepares  $|n=1\rangle$ , we apply the frequency-conversion drive at  $\omega_{cr} = \omega_b - \omega_a$  for a variable time  $\Delta t$ , and perform dispersive readout. **b**, Dependence of Fock-qubit  $|n=1\rangle$  population ( $P_1$ ) on  $\Delta t$  for the pulse sequence in **a**. Open blue circles are measured data and the solid black line is a fit based on equation (S14). **c**, Pulse sequence to test the QND-ness of the cat-quadrature readout: We prepare  $|\mathcal{C}_\alpha^+\rangle$ , and perform two successive cat-quadrature readout pulses. **d**, Histogram of second readout postselected on the indicated result  $|\pm\alpha\rangle$  of the first measurement. Open yellow (green) circles are measured data after finding  $|\pm\alpha\rangle$  ( $|- \alpha\rangle$ ) on the first measurement. Solid lines are Gaussian fits.

#### D. QND-ness

An important property of a qubit readout is to be quantum non-demolition (QND). We test the QND-ness of the cat-quadrature readout by preparing  $|\mathcal{C}_\alpha^+\rangle$  and performing two cat-quadrature readout pulses one after the other as shown in the pulse sequence Fig. S6c. The result of the first measurement generates histograms much like the bottom panel of Fig. 4a. We postselect on the outcomes  $|\pm\alpha\rangle$  for this first measurement using a stringent threshold. In Fig. S6d, we plot the two histograms showing the outcomes of the second measurement contingent on this postselection. The I-axis is scaled by the  $\sigma$  of the first measurement, and we find the second measurement has a 10% larger  $\sigma$  given by the Gaussian fit (solid). We calculate the QND-ness  $\mathcal{Q} = (p(+\alpha|+\alpha) + p(-\alpha|-\alpha))/2 = 0.85$ , where  $p(\pm\alpha|\pm\alpha)$  are the probabilities of the respective second measurement outcome conditioned on the first measurement [17]. We note that the conversion process leads to a significantly decreased effective lifetime of the nonlinear resonator such that the phase flip rate due to single-photon loss becomes non-negligible in spite of the suppression factor  $(p^{-1} - p)/2 \approx 0.006$  for  $\bar{n} = 2.6$  (see section I). In order to quantify this effect, we simulate the master equation

$$\dot{\hat{\rho}} = -\frac{i}{\hbar}[\hat{H}_{cat} + \hat{H}_{cr}, \hat{\rho}] + \kappa_b \mathcal{D}[\hat{b}]\hat{\rho},$$

where the two Hamiltonian terms correspond to equations (1) and (3) of the main text and  $\mathcal{D}[\mathcal{O}]\hat{\rho} = \mathcal{O}\hat{\rho}\mathcal{O}^\dagger - \frac{1}{2}\mathcal{O}^\dagger\mathcal{O}\hat{\rho} - \frac{1}{2}\hat{\rho}\mathcal{O}^\dagger\mathcal{O}$ . Here we do not include decoherence of the nonlinear resonator. This yields a QND-ness of  $\mathcal{Q} = 0.93$ . If we add the additional decoherence terms present in equation (S21) and use the parameters  $n_{th} = 0.08$  and  $\kappa_{\phi,eff}/2\pi = 230$  Hz (see section XI) we find  $\mathcal{Q} = 0.90$ . We expect an additional reduction of the measured QND-ness with respect to this value due to the finite separation of the histograms even in absence of additional phase-flips. These effects will be the topic of further study. A linear increase in the photon number exponentially suppresses these spurious effects [1], meaning that an increase in QND-ness (and also readout fidelity) should come with the mitigation of the drive-power-dependent heating (see section XI) in future iterations of this system.

#### X. COHERENCE MEASUREMENTS USING DISPERSIVE READOUT

In this section we measure the coherence properties presented in Fig. 4 of the main text in a complementary way by mapping the back onto the Fock qubit and performing dispersive readout. We additionally discuss leakage to states outside the cat qubit encoding.

We measure the coherence time of the states along the Z- and Y-axis of the cat qubit using dispersive readout as shown in Fig. S7a, c: First, we initialize the Kerr-cat qubit in the state  $|\mathcal{C}_\alpha^+\rangle$  by ramping on the squeezing drive. Then we apply one of four operations ( $X(0)=\mathbb{1}$ ,  $X(\pi)$ ,  $X(\pi/2)$ , and  $X(-\pi/2)$ ) leaving the cat qubit in the state  $|\mathcal{C}_\alpha^+\rangle$ ,  $|\mathcal{C}_\alpha^-\rangle$ ,  $|\mathcal{C}_\alpha^{-i}\rangle$ , and  $|\mathcal{C}_\alpha^{+i}\rangle$  respectively. After a variable wait time  $\Delta t$ , we perform another set of operations to reorient the cat qubit along its Z-axis, map back onto the Fock qubit and read out dispersively. In order to symmetrize the readout contrast, we apply the return-operations  $X(0)$  as well as  $X(\pi)$  for each of the first two states and  $X(\pi/2)$

as well as  $X(-\pi/2)$  for each of the second two states and take the difference between the thresholded measurement results. In all four obtained datasets (see Fig. S7b and Fig. S7d) we observe an exponential decay with respective decay times:  $2.62 \mu\text{s} \pm 0.06 \mu\text{s}$ ,  $2.56 \mu\text{s} \pm 0.05 \mu\text{s}$ ,  $2.53 \mu\text{s} \pm 0.05 \mu\text{s}$ , and  $2.61 \mu\text{s} \pm 0.05 \mu\text{s}$  corresponding well to the decay times observed when using the cat-quadrature readout.

We measure the lifetime of the coherent states  $|\pm\alpha\rangle$  by first initializing the Fock qubit along the X-axis with a  $Y(\pm\pi/2)$  operation, then mapping onto the Kerr-cat qubit, waiting for a variable time  $\Delta t$ , mapping back onto the Fock qubit and finally performing a second  $Y(\pm\pi/2)$  operation followed by dispersive readout. The second pulse is performed with a software detuning leading to the oscillations visible in the datasets shown in Fig. S7f. We show only the oscillating population of the  $|0\rangle$  state for  $|+\alpha\rangle$  to avoid redundancy. The two sets of blue dots in the figure correspond to different detunings. Note that here we do not symmetrize the measurement and the curve decays to a value other than 0.5, as expected because of leakage to higher excited states. Therefore, we do not fit it with an exponential decay. We can however mark the time at which its contrast has been reduced by a factor  $e^{-1}$ . This happens at  $T_{e-1} \approx 110 \mu\text{s}$  corresponding well to the timescale found with cat-quadrature readout.

The dispersive measurement used here also gives us access to the populations of the higher excited states of the Fock qubit at the end of the experiment which reflect the leakage out of the cat-encoding space (see section III). We plot the population fraction of the states  $|n > 1\rangle$  as red dots in the figure. Small oscillations of this curve indicate a small error in the thresholding regions used in our single-shot measurement, but do not change the overall behavior. The curve indicates an increase and saturation of the population of higher excited states with a characteristic time  $T_{>1} \approx 21 \mu\text{s} \pm 2 \mu\text{s}$ . The same quantities are plotted for the coherence measurements of  $|\mathcal{C}_\alpha^+\rangle$  and  $|\mathcal{C}_\alpha^i\rangle$  in Fig. S7g and Fig. S7h. The curves for  $|\mathcal{C}_\alpha^-\rangle$  and  $|\mathcal{C}_\alpha^{+i}\rangle$  are very similar and are not shown. The constant offset in population is due to a small threshold error attributing some  $|0\rangle$  and  $|1\rangle$  state population to the  $|> 1\rangle$  states and does not affect the overall behavior of the curve as a function of  $\Delta t$ . An exponential fit to the data for all four states ( $|\mathcal{C}_\alpha^+\rangle$ ,  $|\mathcal{C}_\alpha^-\rangle$ ,  $|\mathcal{C}_\alpha^{+i}\rangle$ , and  $|\mathcal{C}_\alpha^{+i}\rangle$ ) gives the respective rise time constants  $14.6 \mu\text{s} \pm 0.8 \mu\text{s}$ ,  $14.1 \mu\text{s} \pm 0.9 \mu\text{s}$ ,  $15.4 \mu\text{s} \pm 1.1 \mu\text{s}$ , and  $14.1 \mu\text{s} \pm 0.8 \mu\text{s}$ .

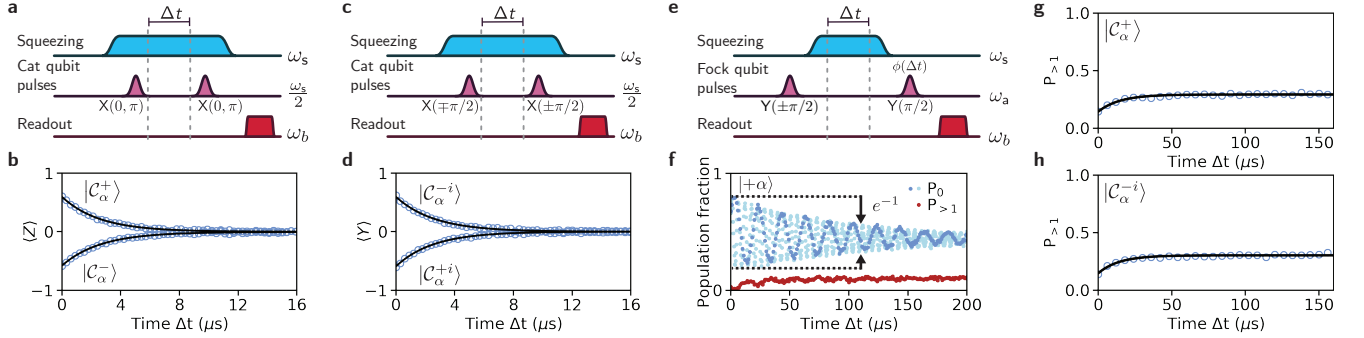


**FIG. S7. Coherence measurements using dispersive readout.** **a,c,** Pulse sequences for measuring the lifetimes of the Schrödinger-cat states along the Z- and Y-axis of the cat qubit. The first set of pulses (respectively  $X(0), X(\pi), X(-\pi/2), X(\pi/2)$ ) initializes the cat qubit in the states  $|\mathcal{C}_\alpha^+\rangle$ ,  $|\mathcal{C}_\alpha^-\rangle$ ,  $|\mathcal{C}_\alpha^{+i}\rangle$ , and  $|\mathcal{C}_\alpha^{+i}\rangle$  followed by a variable wait time  $\Delta t$ . The second set is used to symmetrize the readout contrast. **b, d** Decay curves of the indicated states. Open blue circles are experimental data, solid black lines are exponential fits with decay times given in the text. **e,** Pulse sequence for measuring the coherent state lifetimes. A  $Y(\pm\pi/2)$  rotation brings the Fock qubit along its X-axis and is followed by mapping onto the cat qubit and a variable wait time  $\Delta t$ . After mapping back, another  $\pi/2$  rotation is applied with a phase  $\phi(\Delta t) = 2\pi f_{\text{det}}\Delta t$ , where  $f_{\text{det}}$  is an effective detuning. **f,** Loss of coherence and leakage to higher excited states as a function of time for initialization in state  $|+\alpha\rangle$ . Blue dots are the evolution of the resulting  $|0\rangle$ -state population of the Fock qubit using an effective detuning of 50 kHz (dark blue) and 200 kHz (light blue). The time  $T_{e-1} \approx 110 \mu\text{s}$  after which the contrast has decreased by a factor  $1/e$  is indicated. Red dots show the population of Fock states  $|n > 1\rangle$  and are offset for clarity. **g, h,** Time-dependence of the population fraction for the Fock states  $|n > 1\rangle$  using the pulse sequences shown in **a** (for  $|\mathcal{C}_\alpha^+\rangle$ ) and **b** (for  $|\mathcal{C}_\alpha^{+i}\rangle$ ). Open blue circles are experimental data, solid black lines are exponential fits with rise times given in the text.

## XI. DECOHERENCE PROCESSES AND LEAKAGE TO HIGHER EXCITED STATES

In this section we will discuss the impact of different decoherence mechanisms on the coherence properties of the presented Kerr-cat qubit. We will first develop analytic expressions in the limit  $p \rightarrow 1$  and for  $\alpha \in \mathbb{R}$ . The action of the annihilation and creation operators on the cat qubit basis states is well approximated by (see section I)

$$\hat{a} |\mathcal{C}_\alpha^\pm\rangle = \alpha |\mathcal{C}_\alpha^\mp\rangle \quad (\text{S15})$$

$$\hat{a}^\dagger |\mathcal{C}_\alpha^\pm\rangle = \alpha |\mathcal{C}_\alpha^\mp\rangle + |\psi_e^\mp\rangle \quad (\text{S16})$$

$$\hat{a} |\mathcal{C}_\alpha^{\mp i}\rangle = \alpha |\mathcal{C}_\alpha^{\pm i}\rangle \quad (\text{S17})$$

$$\hat{a}^\dagger |\mathcal{C}_\alpha^{\mp i}\rangle = \alpha |\mathcal{C}_\alpha^{\pm i}\rangle + |\psi_e^{\pm i}\rangle \quad (\text{S18})$$

$$\hat{a} |\pm\alpha\rangle = \pm\alpha |\pm\alpha\rangle \quad (\text{S19})$$

$$\hat{a}^\dagger |\pm\alpha\rangle = \pm\alpha |\pm\alpha\rangle + D(\pm\alpha) |1\rangle \quad (\text{S20})$$

where the states  $|\psi_e^\mp\rangle = (D(\alpha) \pm D(-\alpha)) |1\rangle$  correspond to the next excited states of the Hamiltonian (1) introduced and spectroscopically measured in section III. In this section we have shown that a coherent drive can only induce transitions from the cat states to the excited states at their difference frequency  $\omega_a - \omega_{\text{gap}}$  in the laboratory frame, with  $\hbar\omega_{\text{gap}} = E_{\text{gap}}$ . Similarly, only  $\hat{a}^\dagger$ -noise with a spectral density around this frequency can cause excitation events. These are usually strongly suppressed as evidenced by the low thermal photon number of the undriven mode. The evolution of the system is described by the master equation

$$\dot{\hat{\rho}} = -\frac{i}{\hbar} [\hat{H}_{\text{cat}}, \hat{\rho}] + \kappa_a (1 + n_{\text{th}}) \mathcal{D}[\hat{a}] \hat{\rho} + \kappa_a n_{\text{th}} \mathcal{D}[\hat{a}^\dagger] \hat{\rho} + \kappa_{\phi, \text{eff}} \mathcal{D}[\hat{a}^\dagger \hat{a}] \hat{\rho}, \quad (\text{S21})$$

where  $\mathcal{D}[\mathcal{O}] \hat{\rho} = \mathcal{O} \hat{\rho} \mathcal{O}^\dagger - \frac{1}{2} \mathcal{O}^\dagger \mathcal{O} \hat{\rho} - \frac{1}{2} \hat{\rho} \mathcal{O}^\dagger \mathcal{O}$ ,  $\kappa_a = 1/T_1$  is the single photon loss rate of the nonlinear resonator,  $n_{\text{th}}$  its equilibrium thermal occupation number, and  $\kappa_{\phi, \text{eff}}$  is an effective dephasing rate.

In this description we use the ideal Hamiltonian  $H_{\text{cat}}$  given in equation (1), because we aim to describe the experiments presented in Fig. 4 where we have accounted for spurious drive-dependent frequency detunings. The effective dephasing rate  $\kappa_{\phi, \text{eff}}$  will be used to give a phenomenological description of the corresponding noise, which in our flux-biased system likely has a  $1/f$  frequency dependence instead of the white noise spectral density assumed here. It is possible to explicitly study the impact of colored noise on this type of qubit [1], but this is outside of the scope of this work.

### A. Photon loss and gain: Bit flips

We will for now neglect leakage to the excited states as well as dephasing noise (setting  $\kappa_{\phi, \text{eff}} = 0$ ) and focus on the effect of photon loss and photon gain within the cat-encoding. In this case both operators only lead to flips of the states on the Z-axis and Y-axis of the cat qubit, while leaving the coherent states on the X-axis invariant.

In the basis of the even and odd cat states with respective populations  $\rho_{00}$  and  $\rho_{11}$  equation (S21) yields the differential equations

$$\begin{aligned} \dot{\rho}_{00}(t) &= \bar{n} \kappa_a (1 + 2n_{\text{th}}) \rho_{11}(t) - \bar{n} \kappa_a (1 + 2n_{\text{th}}) \rho_{00}(t) \\ \dot{\rho}_{11}(t) &= \bar{n} \kappa_a (1 + 2n_{\text{th}}) \rho_{00}(t) - \bar{n} \kappa_a (1 + 2n_{\text{th}}) \rho_{11}(t) \end{aligned}$$

with the solutions

$$\begin{aligned} \rho_{00}(t) &= \frac{1}{2} + \frac{1}{2} (\rho_{00}(0) - \rho_{11}(0)) e^{-2\bar{n} \kappa_a (1 + 2n_{\text{th}}) t} \\ \rho_{11}(t) &= \frac{1}{2} - \frac{1}{2} (\rho_{00}(0) - \rho_{11}(0)) e^{-2\bar{n} \kappa_a (1 + 2n_{\text{th}}) t} \end{aligned}$$

These expressions show the action of the bit flip channel where any initial state decays to an equal statistical mixture of even and odd cat states with a time constant given by  $2\bar{n} \kappa_a (1 + 2n_{\text{th}})$ , where  $\bar{n} = \alpha^2$  is the average photon number in the cat state. The same result is found for the flips between the states  $|\mathcal{C}_\alpha^{\mp i}\rangle$ . Using the measured thermal photon number  $n_{\text{th}} = 0.04$  we would expect a bit-flip time of  $\approx 2.8 \mu\text{s}$  which is slightly larger than the experimentally measured values. Heating to a value of  $n_{\text{th}} = 0.08$  (yielding  $\approx 2.6 \mu\text{s}$ ) due to the application of the drives [10] could account for this difference.



### B. Photon gain: Leakage to higher excited states and phase flips

The definitions given in equations (S20-S21) indicate that the process  $\kappa_a n_{\text{th}} \mathcal{D}[\hat{a}^\dagger]$ , which causes leakage from the cat states to the excited states, happens at a rate  $\kappa_a n_{\text{th}}$ . We now focus on the timescale over which the corresponding populations equilibrate (as measured in Fig. S7). In the approximation  $n_{\text{th}} \ll 1$ , the rate equations for the population  $p_c$  of the cat states and the population  $p_e$  of the first two excited states ( $|\psi_e^\pm\rangle$ ) are given by:

$$\begin{aligned}\dot{p}_e(t) &= \kappa_a n_{\text{th}} p_c(t) - \kappa_a (1 + n_{\text{th}}) p_e(t) \\ \dot{p}_c(t) &= -\kappa_a n_{\text{th}} p_c(t) + \kappa_a (1 + n_{\text{th}}) p_e(t)\end{aligned}$$

which we solve with the initial conditions  $p_c(0) = 1$  and  $p_e(0) = 0$ . This results in a time-dependence of the populations given by

$$\begin{aligned}p_e(t) &= \frac{n_{\text{th}}}{1 + 2n_{\text{th}}} (1 - e^{-\kappa_a (1 + 2n_{\text{th}}) t}) \\ p_c(t) &= \frac{1}{1 + 2n_{\text{th}}} + \frac{n_{\text{th}}}{1 + 2n_{\text{th}}} (1 + e^{-\kappa_a (1 + 2n_{\text{th}}) t})\end{aligned}$$

indicating that they reach equilibrium on a timescale of  $1/(\kappa_a (1 + 2n_{\text{th}})) \approx 14 \mu\text{s}$ . This gives the correct order of magnitude, while underestimating the timescale found in experiment.

Finally, we note that for the photon number  $\bar{n} = 2.6$  demonstrated in this work the excited states are above the energy barrier shown in Fig. S1. This means that the excited states do not benefit from the same suppression of phase flips as the cat states. We therefore expect that thermal jumps to these excited states contribute significantly to the observed phase-flip rate.

### C. Dephasing: Leakage to higher excited states and phase flips

We have so far neglected dephasing noise described by  $\kappa_{\phi, \text{eff}} \mathcal{D}[\hat{a}^\dagger \hat{a}]$ . In this section, we will discuss its influence qualitatively, while in the next section we will investigate it further through numerical simulations.

The effect of this type of noise within the cat Bloch sphere can be understood by adding a term  $\Delta \hat{a}^\dagger \hat{a}$  to the Kerr-cat Hamiltonian (1), where  $\Delta$  is some unknown fluctuating quantity with a spectral density of fluctuations given by the environmental noise. We analyze the effect of this noisy Hamiltonian term in two parts: rotations within the cat Bloch sphere, and leakage to higher excited states. Firstly, projected in the cat-qubit basis, this Hamiltonian reduces to  $\Omega_z \hat{\sigma}_z$  where the Rabi rate around the Z-axis is  $\Omega_z = -4\Delta |\alpha|^2 e^{-2|\alpha|^2}$  [2]. This shows that the susceptibility of the cat qubit to *any* frequency of  $\hat{a}^\dagger \hat{a}$  noise is exponentially suppressed. Furthermore, we do not expect this noise to contribute to the bit flip rate, because the underlying operator conserves parity.

Additionally, the operator  $\hat{a}^\dagger \hat{a}$  can also cause leakage to the excited states, which leads to dephasing of the cat qubit for our experimental parameters as discussed in the previous section. It can be shown [1], that such leakage only occurs for noise with a spectral density around the gap frequency  $\omega_{\text{gap}}$ . This can be understood in a similar manner to the effect of a spin-locking experiment where a driven qubit becomes sensitive to noise only around the induced Rabi frequency [18].

In our experiment we observe a reduction of the overall susceptibility to dephasing noise of the Kerr-cat qubit with respect to the Fock qubit as evidenced by the increase of the respective transverse decoherence times along the qubit X-axis.

### D. Numerical simulation

In this section we simulate the evolution of the states on the six cardinal points of the cat-qubit Bloch sphere according to the master equation (S21) and compare it to the data presented in Fig. 4 of the main text. We use the independently determined values of  $K$  and  $\epsilon_2$ , but vary both  $n_{\text{th}}$  and  $\kappa_{\phi, \text{eff}}$  to investigate the effect of these parameters on the predicted coherence properties.

We start out with  $\kappa_{\phi, \text{eff}} = 0$  meaning that we neglect the suppressed impact of the dephasing noise as well as potential leakage due to this noise process. We observe that for a value of  $n_{\text{th}} = 0.04$ , corresponding to the measured value in the undriven system, our simulation overestimates both the bit-flip and phase-flip times. An increase to a value of  $n_{\text{th}} = 0.08$  yields the correct bit-flip time as expected from our prior analysis, but does not reproduce the phase-flip time.

A reasonably good agreement can only be found for a value of  $n_{\text{th}} = 0.12$  as shown in Fig. S8. In panels **a**, **b**, and **c** of the figure we compare the experimental data to the simulation results. To this end, we scale the latter to the readout contrast of the former. The simulation finds a bit-flip time of  $\approx 2.4 \mu\text{s}$  and a phase-flip time of  $\approx 130 \mu\text{s}$ , thus very slightly underestimating the former while overestimating the latter. In Fig. S8d we compare the leakage to the excited states found in simulation by evaluating  $1 - \text{tr}(|\mathcal{C}_\alpha^+\rangle\langle\mathcal{C}_\alpha^+|\hat{\rho}) - \text{tr}(|\mathcal{C}_\alpha^-\rangle\langle\mathcal{C}_\alpha^-|\hat{\rho})$  to the average of the measured  $P_{>1}$ -datasets presented in section X. As described in this section, we attribute the offset in the data to an imprecision in the thresholding of the single-shot measurement that does not change the rise-time or overall scaling of the population increase. In order to compare simulation to experiment we therefore offset the simulation result such that it matches the data at time  $\Delta t = 0$ , but do not rescale it. The leakage rise time is found to be  $\approx 16 \mu\text{s}$ . The population increase is slightly smaller than found in the experiment.

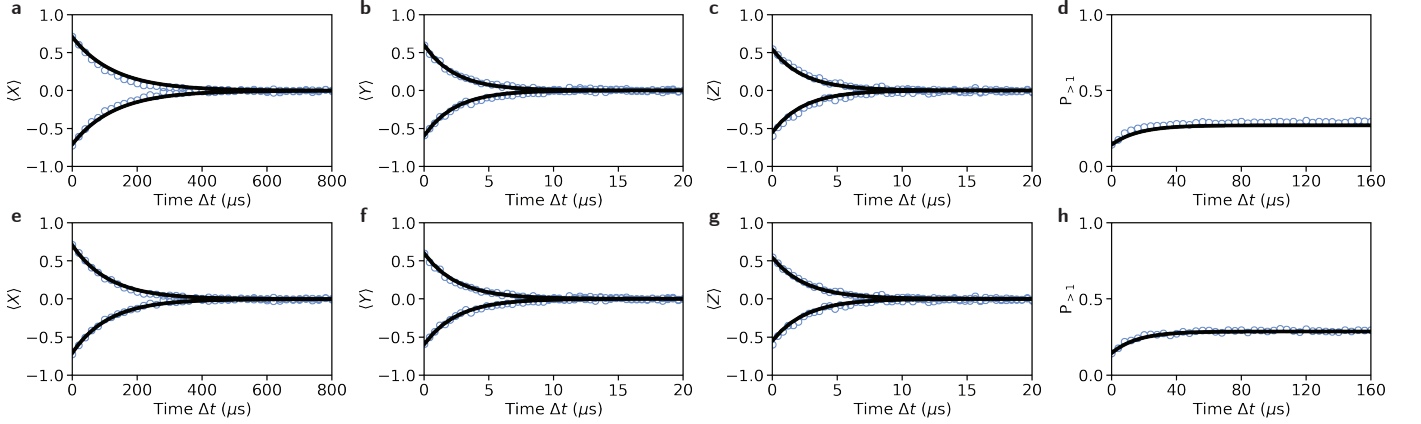


FIG. S8. **Comparison of simulated decoherence to data.** **a,b,c**, Decay curves of the cat-qubit states  $|\pm X\rangle$ ,  $|\pm Y\rangle$ , and  $|\pm Z\rangle$ . Open blue circles are the data presented in Fig. 4. Solid black lines are the corresponding expectation values of the cat-qubit state found from simulation of equation (S21) for  $n_{\text{th}} = 0.12$  and  $\kappa_{\phi,\text{eff}}/2\pi = 0$  and scaled to match the experimental measurement contrast. **d**, Increase of the excited state population. Open blue circles are data shown in Fig. S7. The solid black line is a simulation  $n_{\text{th}} = 0.12$  and  $\kappa_{\phi,\text{eff}}/2\pi = 0$ , offset to match the value of the data at  $\Delta t = 0$ , but not scaled. **e,f,g**, Same experimental data as in **a,b,c**. Simulation results were obtained for  $n_{\text{th}} = 0.08$  and  $\kappa_{\phi,\text{eff}}/2\pi = 230 \text{ Hz}$  and scaled to match the measurement contrast. **h**, Same experimental data as in **d**. Simulation data is shown for  $n_{\text{th}} = 0.08$  and  $\kappa_{\phi,\text{eff}}/2\pi = 230 \text{ Hz}$ , offset but not scaled.

In a second simulation we choose the value  $n_{\text{th}} = 0.08$  which we expect for the measured bit-flip time and add a small amount of effective dephasing noise with  $\kappa_{\phi,\text{eff}}/2\pi = 230 \text{ Hz}$ . The corresponding simulation results reproduce the data well with a bit-flip time of  $\approx 2.6 \mu\text{s}$ , a phase-flip time of  $\approx 110 \mu\text{s}$  and a leakage rise time of  $\approx 16 \mu\text{s}$ . They are presented in Fig. S8e,f,g,h.

While these results are only based on a phenomenological description of the system (in particular with regard to the fact that the spectral-density of the dephasing noise in our experiment is most likely not uniform) they do give an intuition on the limiting factors in the current experiment. It seems probable that a large part of the remaining phase flips comes from a combination of leakage to states outside of the cat encoding and the fact that these states are above the energy barrier. Strategies to reduce the impact of this effect include increasing the ratio between  $g_3$  and  $K$  in order to reduce effective pump strengths, as well as introducing two-photon dissipation [1, 7, 19] to counteract the heating. An increase in photon number by a factor of two would bring the first excited states below the energy barrier [1] and, combined with the previously mentioned strategies, would make the system insensitive to leakage to these levels. A more in-depth study of these effects as a function of  $\alpha$  will be the topic of future work.

- 
- [1] S. Puri, A. Grimm, P. Campagne-Ibarcq, A. Eickbusch, K. Noh, G. Roberts, L. Jiang, M. Mirrahimi, M. H. Devoret, and S. M. Girvin, *Phys. Rev. X* **9**, 041009 (2019).
  - [2] S. Puri, S. Boutin, and A. Blais, *Npj Quantum Inf.* **3**, 18 (2017).
  - [3] J. Guillaud and M. Mirrahimi, *Phys. Rev. X* **9**, 041053 (2019).
  - [4] R. Lescanne, M. Villiers, T. Peronnin, A. Sarlette, M. Delbecq, B. Huard, T. Kontos, M. Mirrahimi, and Z. Leghtas, *Nature Physics* (2020).
  - [5] M. Nielsen and I. Chuang, *Quantum Computation and Quantum Information* (Cambridge University Press, 2000).
  - [6] N. E. Frattini, V. V. Sivak, A. Lingenfelter, S. Shankar, and M. H. Devoret, *Phys. Rev. Applied* **10**, 054020 (2018).

- [7] Z. Leghtas, S. Touzard, I. M. Pop, A. Kou, B. Vlastakis, A. Petrenko, K. M. Sliwa, A. Narla, S. Shankar, M. J. Hatridge, et al., *Science* **347**, 853 (2015).
- [8] J. M. Chow, J. M. Gambetta, A. D. Córcoles, S. T. Merkel, J. A. Smolin, C. Rigetti, S. Poletto, G. A. Keefe, M. B. Rothwell, J. R. Rozen, et al., *Phys. Rev. Lett.* **109**, 060501 (2012).
- [9] S. Touzard, A. Grimm, Z. Leghtas, S. Mundhada, P. Reinhold, C. Axline, M. Reagor, K. Chou, J. Blumoff, K. Sliwa, et al., *Phys. Rev. X* **8**, 021005 (2018).
- [10] D. Sank, Z. Chen, M. Khezri, J. Kelly, R. Barends, B. Campbell, Y. Chen, B. Chiaro, A. Dunsworth, A. Fowler, et al., *Phys. Rev. Lett.* **117**, 190503 (2016).
- [11] S. E. Nigg, H. Paik, B. Vlastakis, G. Kirchmair, S. Shankar, L. Frunzio, M. H. Devoret, R. J. Schoelkopf, and S. M. Girvin, *Phys. Rev. Lett.* **108** (20).
- [12] N. E. Frattini, U. Vool, S. Shankar, A. Narla, K. M. Sliwa, and M. H. Devoret, *Appl. Phys. Lett.* **110**, 222603 (2017).
- [13] P. Campagne-Ibarcq, E. Zayats-Geller, A. Narla, S. Shankar, P. Reinhold, L. Burkhardt, C. Axline, W. Pfaff, L. Frunzio, R. Schoelkopf, et al., *Phys. Rev. Lett.* **120**, 200501 (2018).
- [14] K. Geerlings, Z. Leghtas, I. M. Pop, S. Shankar, L. Frunzio, R. J. Schoelkopf, M. Mirrahimi, and M. H. Devoret, *Phys. Rev. Lett.* **110**, 120501 (2013).
- [15] W. Pfaff, C. J. Axline, L. D. Burkhardt, U. Vool, P. Reinhold, L. Frunzio, L. Jiang, M. H. Devoret, and R. J. Schoelkopf, *Nature Physics* **13** (2017).
- [16] J. Gambetta, W. A. Braff, A. Wallraff, S. M. Girvin, and R. J. Schoelkopf, *Phys. Rev. A* **76**, 012325 (2007).
- [17] S. Touzard, A. Kou, N. E. Frattini, V. V. Sivak, S. Puri, A. Grimm, L. Frunzio, S. Shankar, and M. H. Devoret, *Phys. Rev. Lett.* **122**, 080502 (2019).
- [18] F. Yan, S. Gustavsson, J. Bylander, X. Jin, F. Yoshihara, D. G. Cory, Y. Nakamura, T. P. Orlando, and W. D. Oliver, *Nature Communications* **4**, 2337 (2013).
- [19] M. Mirrahimi, Z. Leghtas, V. V. Albert, S. Touzard, R. J. Schoelkopf, L. Jiang, and M. H. Devoret, *New J. Phys.* **16**, 045014 (2014).